NASA CR-66176

LUNAR SIMULATION MODEL AND OPTICAL STUDIES FOR LUNAR ORBITER SYSTEM SUPPORT

By H. Graboske and E. Marsh

September 1966

BSR 1362

Prepared under Contract No. NAS1-5710 by
Bendix Systems Division
Ann Arbor, Michigan

for

NATIONAL AERONAUTICS AND SPACE ADMINISTRATION

CONTENTS

ILLUSTRATIONS

TABLES

ABSTRACT

The construction, calibration and analysis of a model which simulates the topographic and photometric characteristics of the lunar surface are described. A quantitative evaluation of the photometric and photogrammetric methods for remotely measuring the topographic features of the lunar surface is made based upon experimental data obtained from the model. Minimum accuracies for photogrammetric measurements, photometric slope and albedo determinations are discussed for several experimental sensor-sun-surface geometries.

author

LUNAR SIMULATION MODEL AND OPTICAL STUDIES FOR LUNAR ORBITER SYSTEM SUPPORT

By H. Graboske and E. Marsh

I. SUMMARY

The purpose of this program is the construction, calibration, and analysis of a model which simulates the topographic and photometric characteristics of the lunar surface. The lunar model is to be used to provide a quantitative evaluation of photometric and photogrammetric methods of remote analysis of lunar surface. The model was designed to simulate the lunar surface closely and has been accurately calibrated topographically and photometrically. The surface normal albedos, the photometric function, and the surface slopes are all known to a high degree of accuracy.

A series of optical studies have been performed using the lunar model under solar illumination, for a variety of source-sensor-target geometries. The minimum accuracies of photogrammetric measurements, photometric slope determinations and albedo determinations have been established. An evaluation of desirable and undesirable experiment geometries has also been made, and comparisons between the Jet Propulsion Laboratory (JPL) mean lunar photometric function, the Hapke theoretical photometric function and the lunar model photometric function have indicated certain operational procedures.

II. INTRODUCTION

Due to the unique manner in which the lunar surface scatters incident light, it is possible to obtain significant information about the topography of the lunar surface by measuring its luminance. In addition to the well established photogrammetric techniques of determining the configuration of an area from photographs, new techniques are being developed for lunar photographic analysis which rely on photometric measurements.

The purpose of this program was the construction of a photometric lunar model which closely simulates the light-scattering properties of the moon, and the use of this model to evaluate the procedures and accuracies of the various methods to be used in remote photographic analysis of the lunar surface. The study portion of the program is in direct support of the Lunar Orbiter photographic experiments, and is designed to produce a quantitative basis for the evaluation of photographic analysis such as will be carried out by the Orbiter and its successors.

The program divides naturally into three phases: design and fabrication of the lunar model; calibration of the model; and optical studies utilizing the complete, calibrated model. The design and fabrication phase of the program required the production of a model which had photometric properties as close to those of the lunar surface as possible. In addition, topographic scale and realistic features were required, as well as a number of special features intended to provide a capability for analyzing the various techniques to be used. The calibration phase consisted of topographic calibration and photometric calibration. The topographic portions required production of an accurate contour map by photogrammetric methods, and the direct measurement of the terraced slopes provided as controls. The photometric calibration required measurement of model albedos and of the photometric functions for the lunar model and a witness model. The third phase, the optical studies, required the generation of photographic data using the calibrated model, and the photographic application of various techniques to the resulting simulated lunar representations. Both photogrammetric and photometric techniques were applied to determine the best operational methods for analyzing these types of data. The limitations, accuracies, and range of validity of the various techniques were also investigated.

Several features should be defined at this point. The geometrical notation used is as follows:

Source plane:	the plane which contains a point at the center of the test area on the model and the path of the source as it moves relative to that point
Sensor plane:	the plane which contains a point at the center of the test area on the model and the path of the sensor as it moves relative to that point
Source angle:	i, the angle between the normal to the target surface and the line from the target to the source. High source angles mean large values of i, so that the source is near the horizon. Low source angles mean small values of i, the source is near the zenith
Sensor angle:	ϵ, the angle between the normal to the target surface and the line from the target to the sensor. High sensor angle means large ϵ, low sensor angle means small ϵ.

Source-sensor/ plane angle: a, the angle between the source plane and the sensor plane. When both source and sensor move in the same plane, a = 0^{o}, which is called the coplanar geometry.

Plase angle: α, the angle between the source-target line and the sensor-target line. The relation between a and α is given by:

$$\cos \alpha = \cos \epsilon \cos i + \sin \epsilon \sin i \cos a$$

Reflectance: the ratio of the light reflected by a surface in a given direction to the light incident on the surface.

Normal albedo: the ratio of the light reflected along the normal to the surface to the light incident on the surface (at a source angle of 0^{o}). The reflectance for direct back-scattering.

Photometric function: the distribution of angular reflectance for a material, as a function of 3 angles, normalized to the reflectance at i = ϵ = 0^{o}. In this study, the three angles used are i, ϵ, and a. The product of the photometric function and the normal albedo gives the reflectance at that angle.

III. MODEL DESCRIPTION

A. Topographic Features

The topographic appearance of the model surface is shown in Figure 1. The overall size of the model surface is 3.6 m by 3.6 m. It consists of a continuous surface having a series of slopes ranging in angle from approximately 0° to 15° on which are superimposed various types of craters, domes, and rills.

The most prominent and numerous type feature displayed is the crater. The craters shown range in diameter from approximately 12 mm to 600 mm. The number of craters of each size varies inversely with the crater size. The craters have an approximate diameter-to-depth ratio of 10:1 for the larger ones down to 3:1 for the smaller ones. Portions of larger craters are included at the front and back edges of the model.

Several domes are also included on the model. Since the domes are not a prominent feature on the lunar surface, only one of each size dome is included on the model. The domes shown have an approximate diameter-to-height ratio of 10:1 and vary in diameter from approximately 18 mm to 180 mm.

Two rills are contained on the model surface. Together the two rills form an approximate arc of 270°, which is designed to produce meaningful and interpretable changes in its appearance at various sensor angles and source angles. The rills vary in width from approximately 150 mm to 240 mm and vary in depth from approximately 22 mm to 30 mm. The sides of the rills have a maximum slope of 26°.

In addition to large scale slopes, several calibrated slopes are provided on the model. These slopes consist of small, flat areas, 22 cm square, set into the surface of the model. They vary in angle from approximately 2° to 15.5° relative to the mean surface of the model.

A witness model was provided for use as a photometric control. The witness model, 0.6 m by 0.6 m square, has the same photometric function as the lunar model, but is flat and without topographic features.

B. Mechanical Features

The model surface is constructed of reinforced molded fiberglass which is covered by a layer of photometric material (Bendix Photomat).

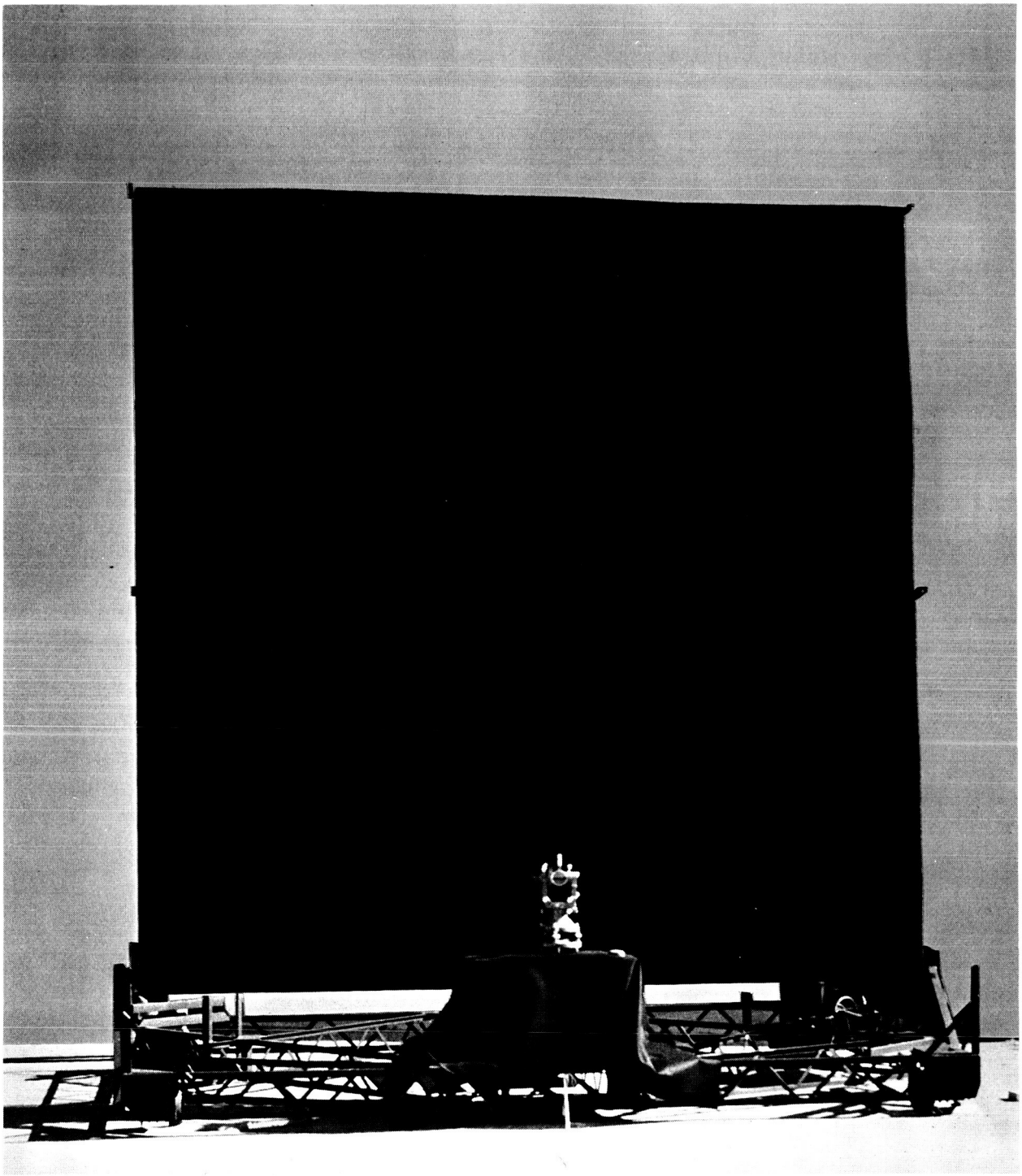

Figure 1 Lunar Model Illuminated by Sunlight

The surface is mounted upon a rigid support structure which is composed of of a table section and a dolly. The table section, to which the model surface is attached, can be varied in inclination from 0^{o} to 90^{o} with respect to the horizontal by a hydraulic system. The total weight of the model sur- and support structure is approximately 318 kg. The mechanical structure of the model is shown in Figure 2.

The simulated lunar surface is made from molded fiberglass. The mold used for the fabrication of the surface was sculptured from a large laminated block of styrofoam plastic. The model surface was then constructed using the mold by applying four layers of fiberglass cloth and epoxy over the mold. After the fiberglass had cured, the top surface was smoothed by sanding.

To produce the desired photometric function for the lunar simulation model, the fiberglass surface was then covered by a layer of Photomat. The first step in this procedure was the application of several coats of 3M optical coating (white) directly on the fiberglass surface. This provided a uniform, almost isotropic reflectance, with an albedo of 90%. Next a 12 mm-thick panel of Scotts industrial foam, 0.8 pores/mm average pore density, was uniformly blackened by several coats of 3M optical coating (black). The blackened foam was then bonded directly to the white fiberglass surface, being carefully molded to the contours of the underlying fiberglass surface.

The model is required to maintain its calibration throughout its useful life to $\pm$ 0.5^{o}. To provide the necessary rigidity combined with ease of handling, the substructure of the model surface is constructed of reinforced fiberglass. The substructure consists of two rectangular box frames 1.8 m by 3.6 m which are approximately 20 cm deep. The rectangular supporting frame and the simulated model surface are given added rigidity by a series of reinforced fiberglass crossmembers.

The support structure assembly is a welded truss-type structure, constructed from extruded aluminum. This type of structure design was selected because it provides the rigidity required to accurately retain the model calibration while being relatively lightweight in comparison to other types of structures having equivalent structural strength. The structure is designed for a maximum deflection of less than 0.25^{o}.

The support assembly consists of a dolly and a movable table. The dolly is equipped with four large-diameter (20 cm) casters which allow

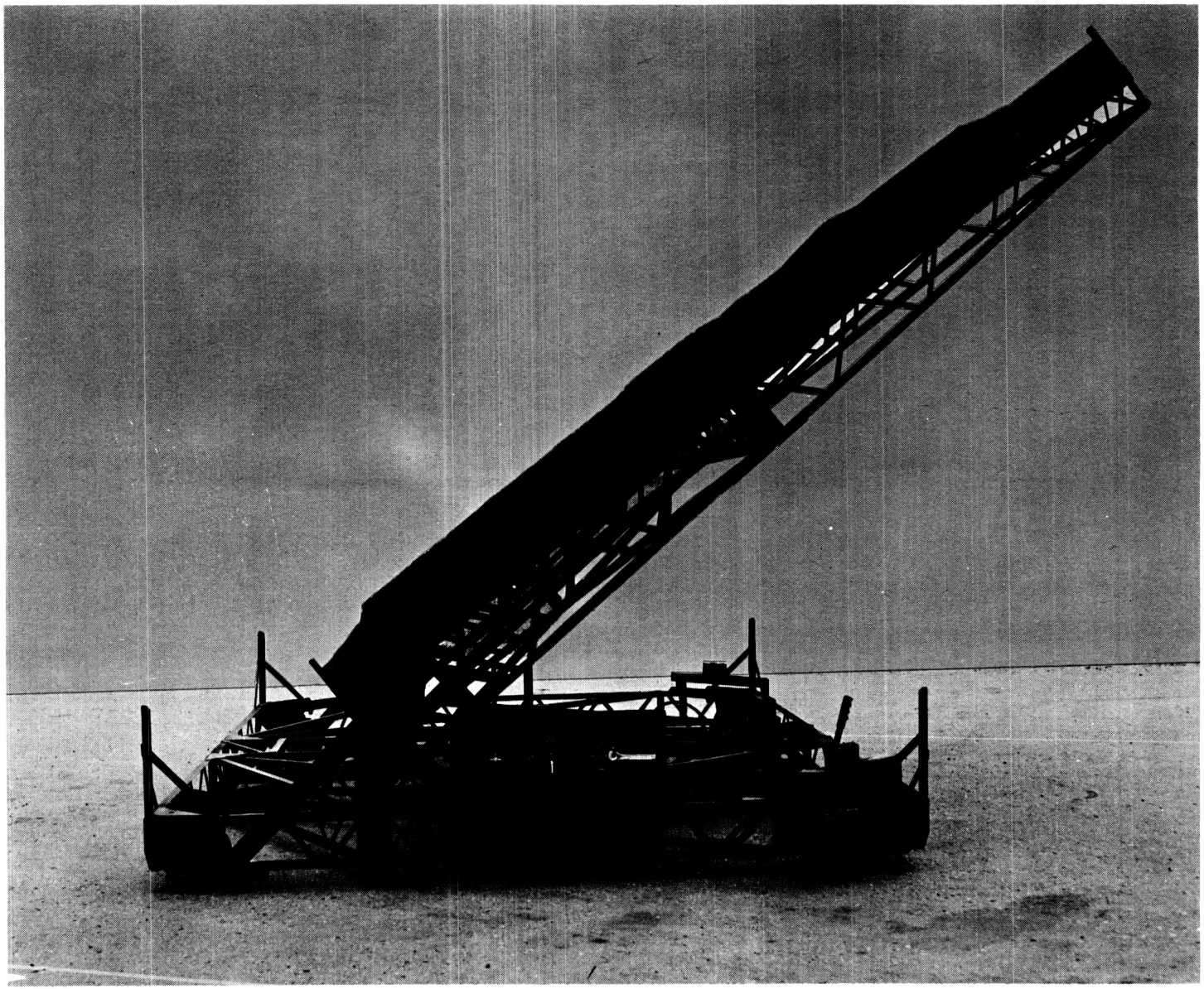

Figure 2 Mechanical Structure of the Lunar Model

the entire assembly to be moved about easily by two or more persons. Screw-jacks are provided at each corner of the dolly for leveling the entire assembly for performing photographic measurements.

The table portion of the support assembly is made in two 1.8 m by 3.6 m sections to facilitate shipment of the model. These sections are bolted together and are disassembled for shipment. Location pads are installed to ensure that the two sections are properly aligned when they are reassembled after shipment.

The table is attached to the dolly at two points by self-aligning bearing blocks. These points are located on the dolly such that no additional ballast is required to stabilize the support assembly regardless of the slope of the model surface.

The slope of the entire table can be varied from 0^{o} to 90^{o} with respect to the horizontal by a hydraulic system which is an integral part of the support assembly. The control panel and the hand pump for the hydraulic system are mounted along one side of the dolly (Figure 2).

A flow diagram for the hydraulic system is shown in Figure 3. The major components are: actuator cylinder, a hand pump, a reservoir, and the related hydraulic valves. Operation of the system is controlled by the three valves located on the control panel and the hand pump which is mounted adjacent to the control panel (Figure 4). The valves located on the control panel are the selector valve, by-pass selector, and a needle valve. The selector valve controls the direction of the table travel and is spring-loaded to return to the closed position when it is released. The by-pass selector is used to direct the flow of fluid through the needle valve for making a vernier adjustment of the table position. The vernier adjustment of table position is controlled by the needle valve. The hand pump is a dual-stroke type and requires a force of approximately 5.5 kg to operate.

The normal operating pressure in the system is approximately 138.0 newtons/cm^2. The system is capable of operating at pressures up to approximately 690 newtons/cm^2 without damage. The pressure relief valve installed in the systems is set at 450 newtons/cm^2.

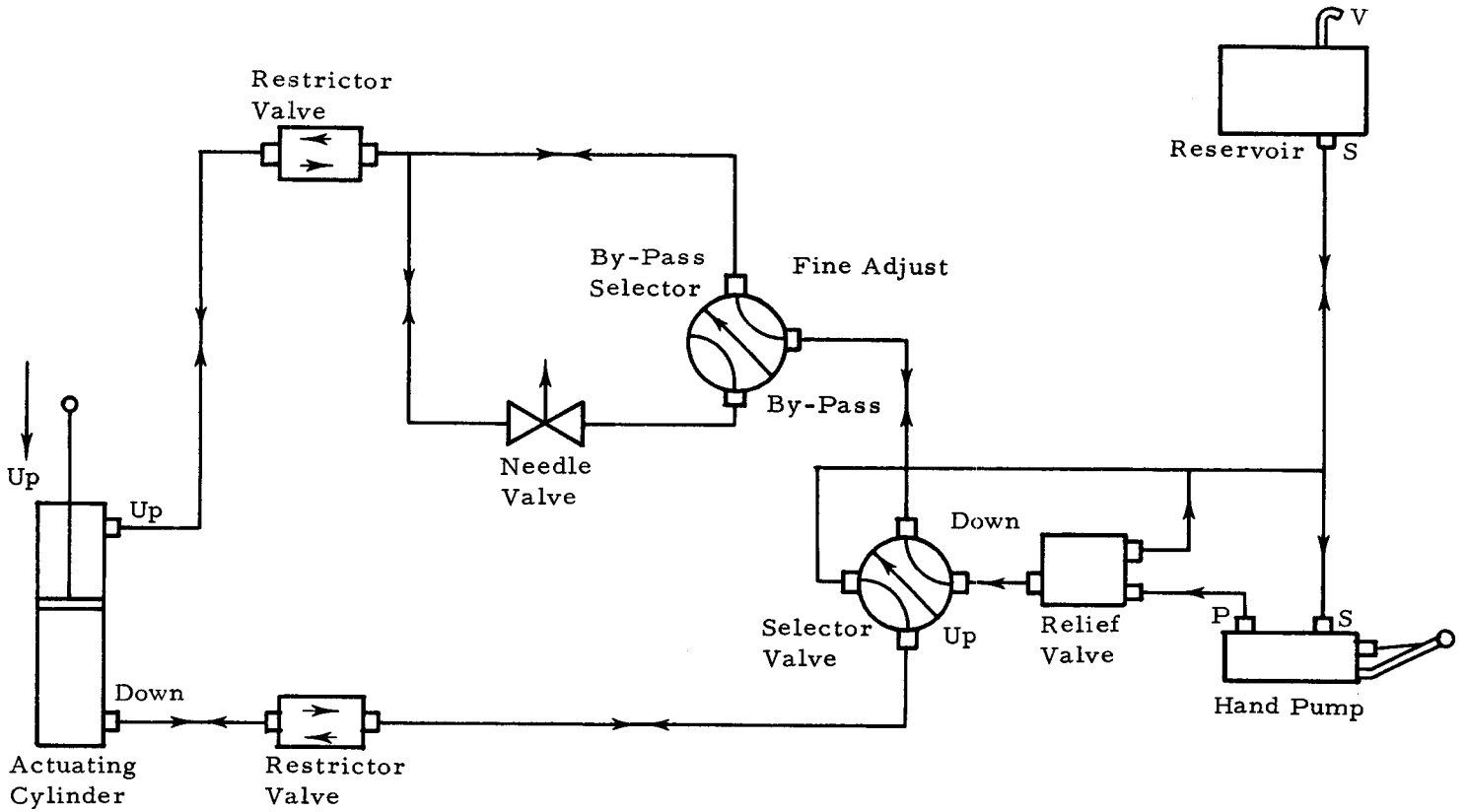

Figure 3 Flow Diagram for Hydraulic System

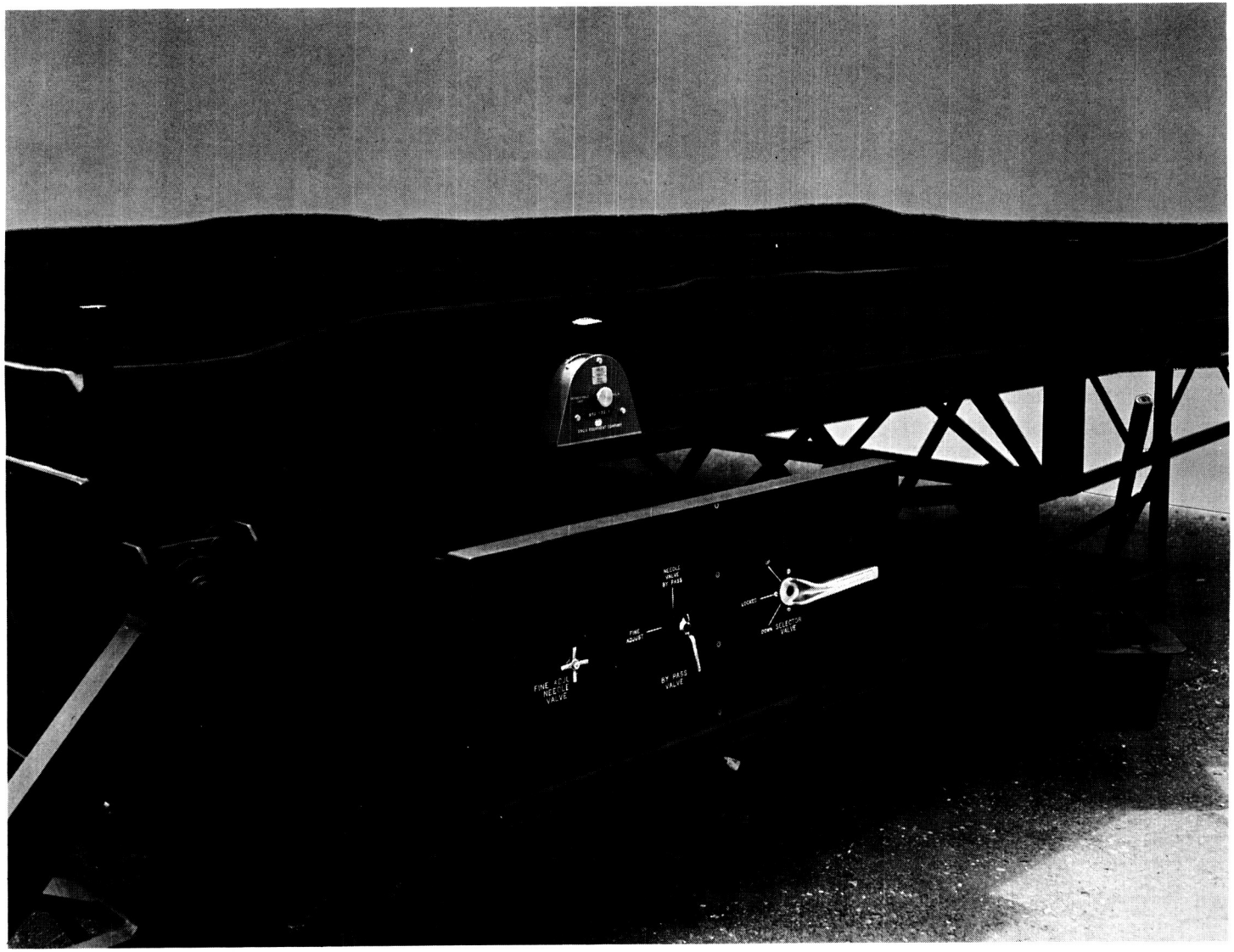

Figure 4 Side View of Model, Showing Support Point, Clinometer on Level Calibration Plate, Hydraulic Pump, and Control Panel

C. Operational Procedure

The model is easily oriented in azimuth by rotating the entire assembly. It can be levelled by adjusting the four screwjacks located at each of the corners of the model. A precision level is placed in turn on both of the level calibration plates, which are reference surfaces aligned to the mean model surface to within an accuracy of ± 12 min of arc. The level is used to indicate the exact horizontal, as the screwjacks are adjusted.

After the model has been accurately levelled in the above manner, the model table can be raised to any elevation angle up to 90°. To do this, the by-pass selector is set at the by-pass position, the selector valve turned to "up" (See Figure 4) and the dual stroke pump operated manually. A clinometer placed on the appropriate level calibration plate (as shown in Figure 4) measures the model table elevation angle with respect to the horizontal. Once the required angle is near, the by-pass selector can be turned to fine adjust, and the very slow fine motion used to move the model table to the exact angle. To return the model table to a horizontal rest position, re-set the by-pass selector to by-pass, and turn the selector valve to "down". For elevations greater than 70°, the hand pump must be used to start the downward motion. For angles less than 70°, the weight of the model table will cause it to settle onto the bumper pads.

The model surface should be protected whenever it is not in use, by placing a large plastic sheet over the entire model area. This reduces the dust, dirt and moisture which can damage the surface, and modify its photometric properties. Small pieces of airborne dirt, especially white flakes can show up quite clearly in photographs. It is recommended that the model surface be cleaned with a powerful vacuum cleaner whenever dust and dirt have accumulated on it. Care should be taken that the vacuum nozzle does not touch the photomat surface or pull the foam away from the substrate. If the model foam surface is damaged or reflectance variations appear, it is possible to restore the original surface by respraying the foam surface with 3M optical black coating. This should be done at low pressure (30 psi or less) and at a very shallow angle to the surface, using broad sweeping arcs. After the respraying, the surface should be vacuumed to remove flakes of air-dried paint which settle on the white substrate.

IV MODEL CALIBRATION

A. Photogrammetric Calibration

A detailed contour map of the lunar model was generated by standard photogrammetric techniques. The model was illuminated by sunlight, the source angle being approximately 60^{o}, high enough to create good contrast without casting shadows that might obscure any part of the model. The model was a vertical orientation, with the photogrammetric baseline 6.1 m away.

A set of six photogrammetric control markers are incorporated in the model which provide a fixed set of vertical and horizontal control points for the photogrammetric reduction. These control markers (two of which are shown in Figure 4) are 15 cm-high posts, 2.2 cm-square cross-section, with an etched cross to provide a sighting point. The exact heights and locations of these markers were measured using a theodolite and steel tape prior to the photographic measurements.

Preliminary studies of the photomat material which is used for the model surface indicated that under certain viewing conditions, it was difficult to focus the stereo plotter on the top surface of the porour photomat. This problem was removed by optimizing the illumination and camera angles.

The photogrammetric data were obtained with a modified Fairchild T12 aerial camera with a 22.8 cm by 22.8 cm film format. The stereo photographs were analyzed by a Galileo-Santoni Model IV stereo cartograph using a 1:16.66 plotting scale to produce a 1:6 scale map. The location of the contour intervals is accurate to within 2.03 mm in the vertical dimension and 0.13 mm in the horizontal dimension.

The results of the photogrammetric calibration are given in Figure 5. This contour map of the entire lunar model has a 1:50 scale, 10-mm contour intervals and 5-mm supplementary contour intervals where rapid surface changes occur. The x and y map coordinates are in mm.

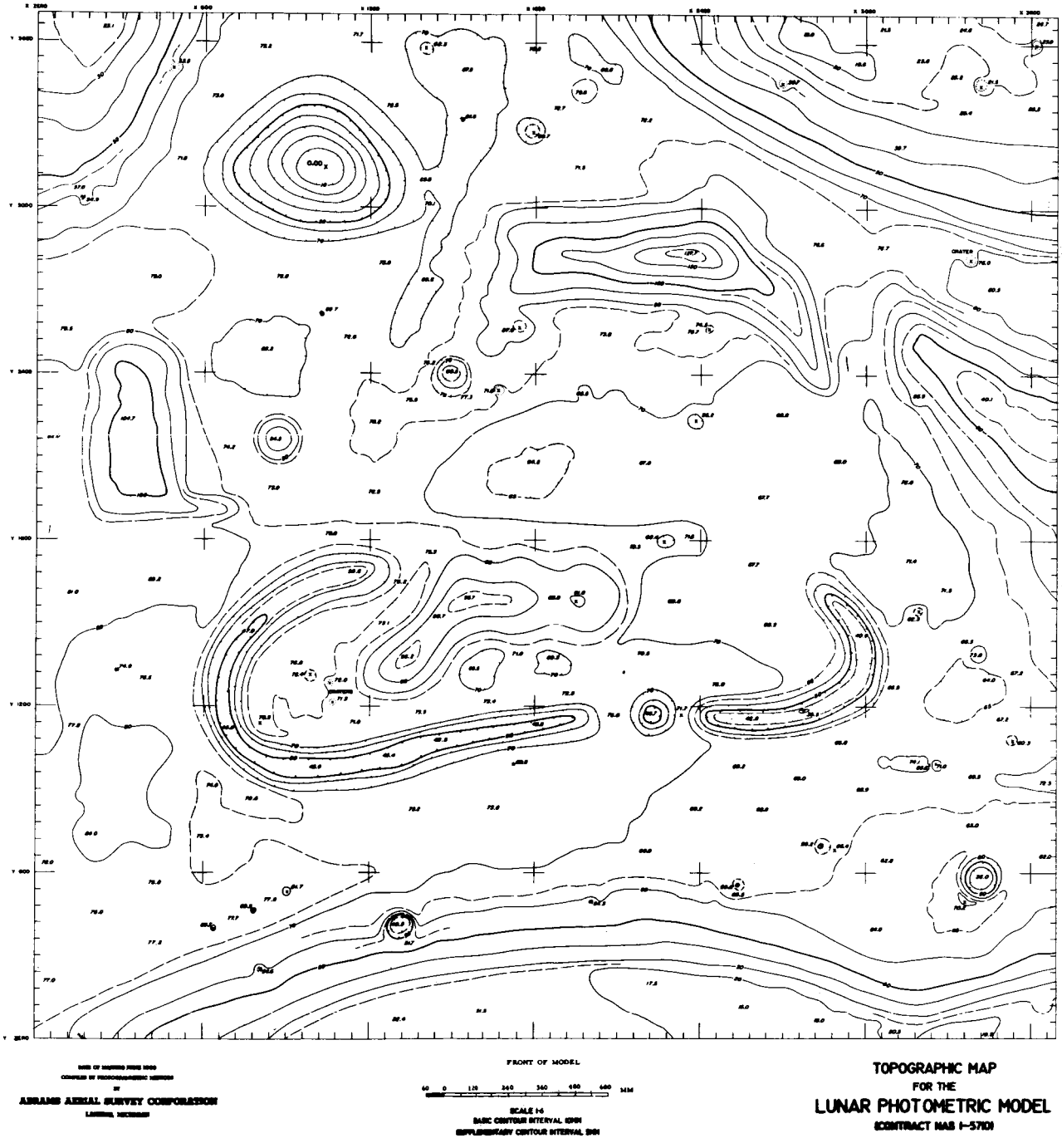

Figure 5 Lunar Model Contour Map

B. Slope Calibration

A set of 20 calibrated slope areas have been provided on the model, each 15 cm square. In addition to the accurate surface calibration given in the contour map presentation, a measurement of the large scale, average slope of these areas was made directly.

The lunar model was set on the leveling pads, and the entire model leveled by use of the control markers and the Wild T3 precision theodolite. The model was leveled to within 0.01° of the horizontal. Once the model was level, the inclination of each slope surface to the horizontal was measured with a Hilger-Watts Model B clinometer. This measurement, accurate to within 1 min of arc (0.017°) was repeated three times. All slopes were measured along the line of steepest descent.

The results of the slope calibration are illustrated in Figure 6. The 14 inclined slope areas range from a minimum of 2.0° to a maximum of 15.5°, oriented in all four directions. In addition, a set of six flat control areas are present which have a slope of 0°, placed at various locations on the model, for the purpose of photometric controls.

The accuracy of the measuring procedure was 1 minute of arc or less ($0^{\circ}.017$), but the individual variations in each slope created larger errors in the final value. These variations, which can be seen in the detailed contour lines on the slope test areas, produced an error of 0.25° in the slope calibration. The values presented in Figure 6 therefore are accurate to $\pm 0.25^{\circ}$, although much higher accuracy can be obtained from the contour intervals of Figure 5. The maximum slope on the model is near the center of the large rill, where the rill wall is inclined 26° to the horizontal.

C. Photometric Calibration

The photometric calibration of the lunar model and the witness model required a large, darkenable facility and a variety of test equipment. The basic test equipment consisted of a collimated light source, a photoelectric photometer, a theodolite, and subsidiary optical equipment.

The light source was a standard theater-type spotlight, with a 500-W lamp, mounted on a tripod. A set of lenses and baffles were

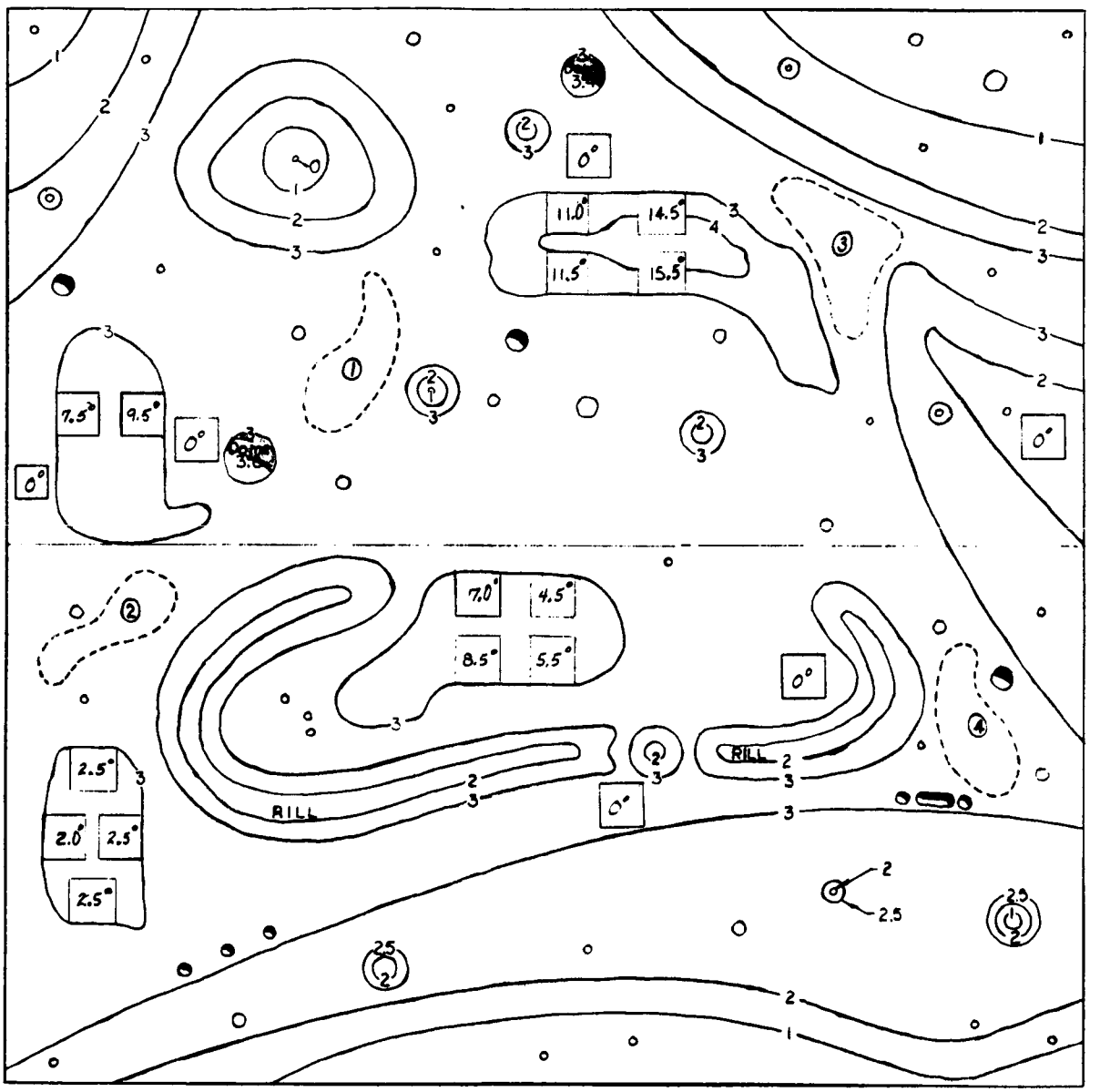

Contour Interval: 2.54 Cm

Scale 1 : 23

Outline of albedo variance areas

Denotes calibrated slopes

Denotes locations of craters

Denotes locations of domes

Figure 6 Lunar Model Slope Calibration Data

attached to provide a 7.6 cm -diameter collimated beam. A plumb bob was suspended from the collimator to allow accurate positioning of the lamp at each of the source stations. The source was operated off a line regulator to ensure constant illumination. The photometer used is a Photo-Research (P-R) brightness meter, with a range of 0.01 to 10^5 ft-L. A calibration standard was used to assure accurate and consistent performance of this device. The collecting optics are 7.6 cm in diameter, with an 0.5° field of view. The accuracy of the instrument is better than 5%. A Wild T3 precision theodolite was used to make all angular measurements, the accuracy of this instrument being better than 5 sec of arc.

The photometric calibration procedure consisted of illuminating the target with the collimated source and measuring the resultant luminance with the P-R brightness meter. The experimental setup is illustrated in Figure 7. Each panel of the lunar model and the witness model was successively mounted on the large movable test stand. The reference baseline for these measurements consisted of three points defined by plumb bobs. The model was placed at the desired height and position and then the entire test stand moved so that the surface of the model was exactly aligned with the plumb bobs. This alignment was determined with the theodolite, which provided an extremely accurate positioning.

Before the calibration procedure was started, the theodolite had been used to sight in two sets of "stations": the source stations, and the sensor stations. The source stations were located on a circle of 1.5 m radius from the central reference point, at 5° intervals.

The sensor stations were located on a larger circle, of 2.8 m radius, also at 5° intervals, from -90° to $+90^{\circ}$ with respect to the normal to the reference baseline. By suspending plumb bobs from both the source and the sensor and aligning both instruments so that these bobs hung exactly over the station markers, it was possible to set the source and sensor angles accurately to within a fraction of a degree. The error in source and sensor angle is negligible compared to the probable error inherent in the photometer reading, which is the major instrumental source of error for the photometric function.

The entire lab was darkened, the brightness of the model when illuminated only by the ambient light being less than the 0.01 ft-L minimum capability of the photometer. The calibration procedure was performed by placing the source at a specified angle (i = source angle,

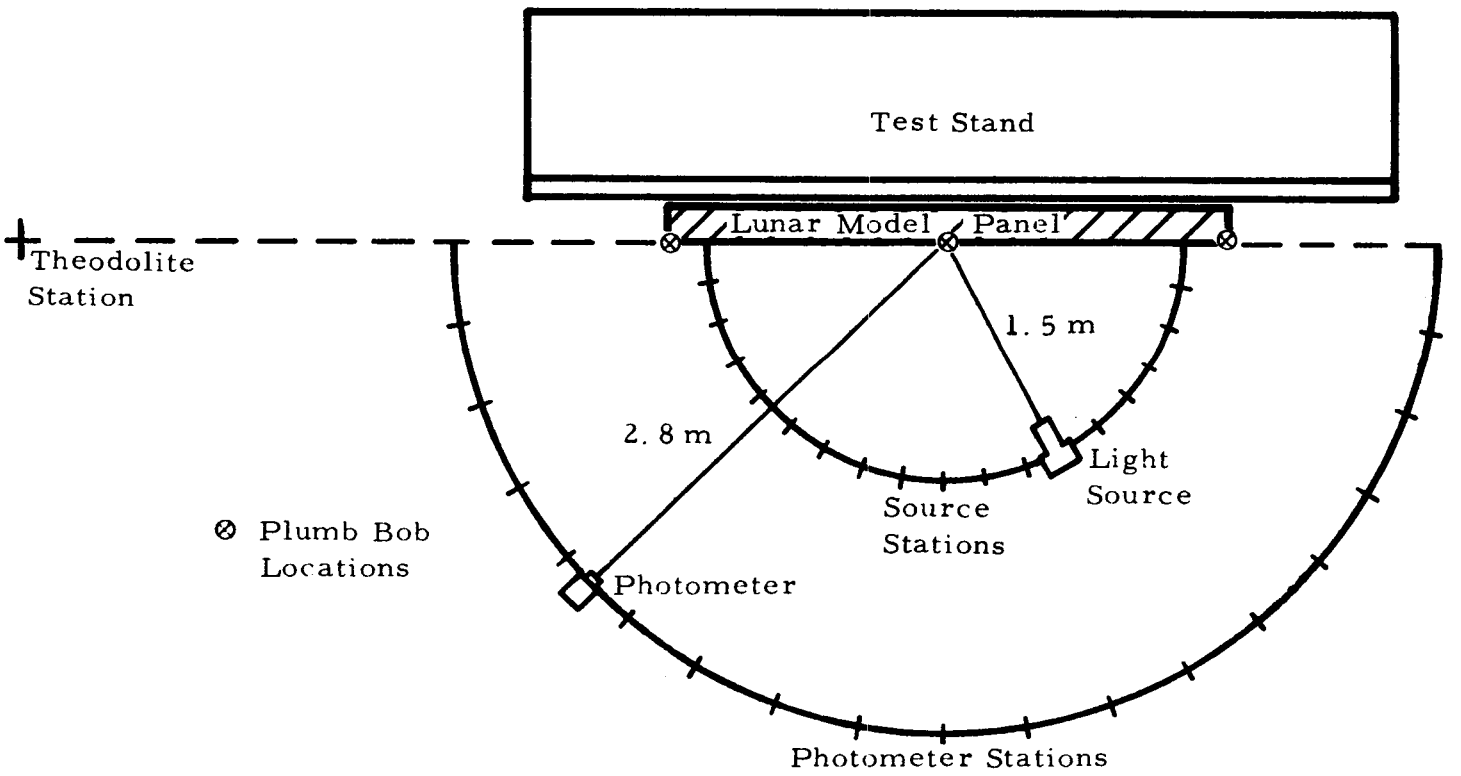

Figure 7 Diagram of Photometric Calibration Instrumentation

ϵ = sensor angle) and illuminating the chosen target areas on the model, which was marked so that the field of view of the photometer would always view the same location. The photometer was then used to perform a series of luminance measurements, covering the complete range of usable sensor angles, usually -80° to $+80^{\circ}$. Due to the severe foreshortening at high sensor angles, the 0.5° field of view would be too large to fit into the foreshortened 7.6 cm spot at source angles above 80°, so these data were not obtained. The sensor readings were obtained at 5° intervals, while the source was positioned at 10° intervals for angles ranging from -80° to $+80^{\circ}$. A magnesium oxide block was used as a reflectance standard to ensure source stability and to provide an absolute luminance calibration. The reflectance of this block was found to be 98%, and its reflectance was approximately lambertian out to 60° with respect to the normal.

Two sets of luminance curves were measured to produce two sets of photometric functions. The first set was measured in a coplanar geometry, where the sensor and the source moved in the same plane (parallel to the ground). This coplanar geometry, where the angle between the source plane and the sensor plane, a, is 0°, is approximately equivalent to the geometry of the sun-moon-earth, all three moving in almost the same plane. The second set of curves were generated for a noncoplanar geometry, the source-sensor plane angle being 90°. Here the source moved in the vertical plane, while the sensor moved in the horizontal plane. In theory, the photometric function for any angle, a, between these two extreme cases could be constructed by interpolating between these two sets of measurements.

The photometric function curves are normalized to 1.0 at the geometry $i = \epsilon = 0^{\circ}$. In practice it is extremely difficult to measure the brightness of an area whenever $i = \epsilon$, because either the source obscures the field of view if in front of the sensor, or the sensor casts a shadow when the source is behind it. For the lunar photometric functions, such as analyzed by Parker et al. (1964), measurements are made at or near eclipse, when the sun is almost aligned with the earth's position, the sensor and source angles almost coinciding. At best this is 1° or more away from the peak, so peak luminances for the moon must be extrapolated, which is rather inaccurate in view of the very rapid change of the lunar photometric function near $i = \epsilon$.

The method chosen for this study involved the use of a beam splitter, placed in front of the source, so that the photometer line of sight could be made to coincide to within minutes of arc with the source beam. This method was used to measure every luminance where $i = \epsilon$, from -80 to +80, as well as for the albedo measurements (see following subsection, "Albedo Calibration"). The beam splitter was calibrated in the laboratory, and gave close to a 50/50 division of the light beam. The apparatus is illustrated in Figure 8. The collimated source illuminated the target area on the lunar model through the beam splitter, for the desired value of i. In addition to illuminating the target area, the source produced a secondary beam, called the sink beam, as well as illuminating the beam splitter. The beam splitter was kept as clean as possible to minimize the light scattering dust particles. The secondary beam was given a much longer path than the target beam, up to 7.6m, to allow diffusion and weakening of the beam. Then a relatively diffuse highly absorbent velvet "light sink" was placed in the sink beam, to minimize back-scatter.

The photometer was placed so that its line of sight coincided exactly with the center of the sink beam and, as viewed through the beam splitter, with the center of the target area. The total luminance of the multiple targets (lunar model, sink surface, and the beam splitter surfaces) was measured. Then the photometer was moved very slightly to the side, just out of the reflected beam from the beam splitter. The two noise sources, the sink and the beam splitter, were found to be nondirectional near the normal to these surfaces, so that a slight change in sensor angle would not cause a measurable change in luminance. This made it possible to read the luminance of the beam splitter alone (slightly off-axis so neither target nor sink were in the field) and of the sink alone (again off-axis so neither the beam splitter or target were in the field). Once these values were obtained, they could be subtracted from the total luminance, yielding the luminance of the target area alone. The luminance at $i = \epsilon$ (the back-scatter peak) had to be scaled for comparison with the normal nonpeak measurements, because the introduction of the beam splitter cut the source intensity by one-half. The magnesium oxide reflectance standard was used for both types of measures (with and without the beam splitter) to give the necessary scale factor. A great deal of care must be taken in the measurement, since the photometric function of a lunar-type surface changes very rapidly near $i = \epsilon$, and a large error can result from a small angular error.

The result of these measurements was a series of luminance values for the lunar model, ranging from -80° to $+80^{\circ}$ in sensor angle in 5° increments, for source angles from -80° to $+80^{\circ}$, in 10° increments, for the two geometries, $a = 0^{\circ}$ and 90°. All these luminances were then

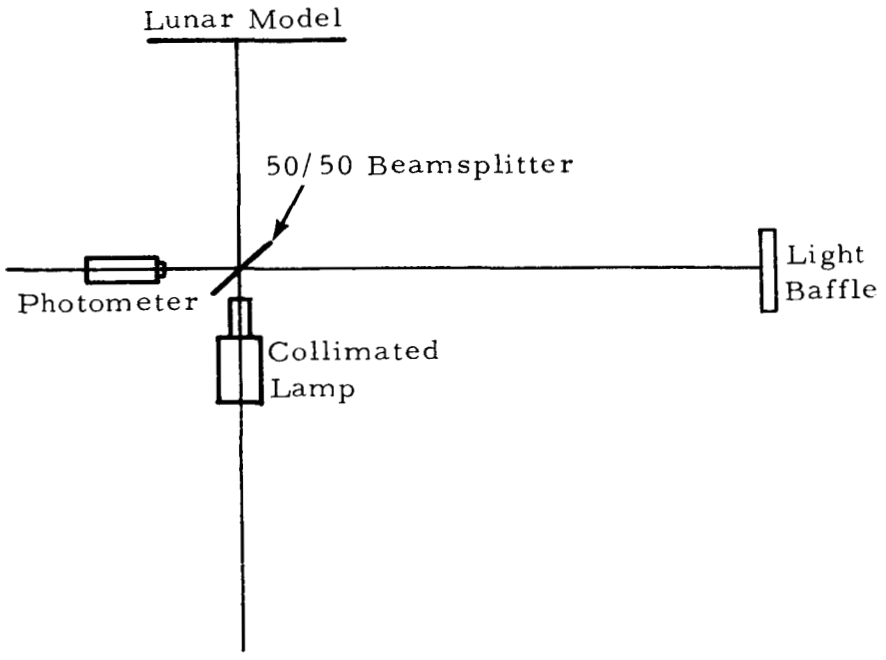

Figure 8 Albedo Measurement Setup

divided by the luminance at $i = \epsilon = 0^{\circ}$ (both source and sensor directly above the target) to obtain the photometric function for this particular area.

The photometric function was determined in this manner for six selected regions on the lunar model, and for two regions on the witness model. The mean differences in the curves for these eight areas were within the estimated accuracy of the photometer (±5%) and were random in character, so all eight sets of photometric function were summed and a mean photometric function computed. The mean photometric function is the same for the lunar model and the witness model and is tabulated in Table I for $a = 0^{\circ}$ and Table II for $a = 90^{\circ}$. The form of these curves is illustrated in Figures 9, 10, and 11.

In general, the coplanar curves exhibit the basic characteristic of the photometric curves of the lunar surface: strong back-scatter with a maximum at $i = \epsilon$, for any value of i. The peaks are very sharp and the luminance falls off rapidly away from the peak in both directions. Even at very high source angles, the back-scattering characteristic is strong. At moderate source angles $30^{\circ} \leq i \leq 60^{\circ}$, the model exhibits a slight forward scattering peak, which is also observed for certain lunar surface areas (Hapke, 1963).

Although the model does exhibit the general behavior found in the lunar surface, there are two major differences which should be noted. First, the peak luminance (at $i = \epsilon$) falls off with increasing source angle. For the lunar case, this does not occur, the value of the photometric function peaking near 1.0 for source angles from 0 to 80°. The lunar model has peak values near 1.0 only for 0° to 10°, with a sharp drop between 20° and 60°, and a leveling off at approximately 0.4 for source angles above 60°. So instead of all the peak values of the photometric function lying near 1.0, they drop off following a bell-shaped curve. This is the major deficiency in the model, producing lower luminances (for all sensor angles) than the lunar surface, for high source angles.

The reason for this behavior is the structure of the Photomat, a porous foam layer with a strongly reflecting substrate. As higher and higher source angles are reached, less of the substrate is visible, due to the longer path of the light rays through the layer of porous foam. Even though the back-scattering characteristics are maintained, the reflectances are lower than the equivalent lunar values for the same geometry.

TABLE I

LUNAR MODEL

COPLANAR PHOTOMETRIC FUNCTION

($a = 0^{o}$)

SENSOR ANGLE (DEG)	SOURCE ANGLES (DEG)																
	80	70	60	50	40	30	20	10	0	-10	-20	-30	-40	-50	-60	-70	-80
85	.344																
80	.349	.339			.203												
75	.236	.364															
70	.159	.385	.300	.296	.226	.190	.146	.109		.062	.045	.047	.049	.063	.074	.115	.098
65		.304	.334						.098	.074							
60	.098	.224	.413	.324	.267	.224	.174	.147	.119	.077	.060	.052	.046	.049	.045	.054	.044
55			.291	.369													
50	.065	.156	.218	.486	.285	.250	.208	.183	.152	.108	.075	.062	.050	.043	.034	.034	.023
45				.345	.326												
40	.046	.115	.164	.270	.589	.290	.242	.221	.194	.145	.106	.080	.059	.042	.028	.024	.014
35					.317	.343							.073				
30	.032	.085	.128	.205	.254	.665	.293	.280	.240	.190	.142	.110	.075	.050	.030	.020	.011
25						.342	.362						.078	.058			
20	.025	.061	.098	.166	.213	.283	.847.	.317	.291	.230	.175	.139	.095	.061	.035	.022	.011
15							.372	.396						.078			
10	.017	.045	.077	.132	.173	.233	.290	.951	.357	.270	.215	.171	.115	.084	.043	.026	.012
5								.405	.429								
0	.014	.033	.057	.103	.148	.205	.243	.321	1.000	.321	.243	.205	.148	.103	.057	.033	.014
-5									.432	.405							
-10	.012	.026	.043	.084	.115	.171	.215	.270	.359	.951	.290	.233	.173	.132	.077	.045	.017
-15				.078						.396	.372						
-20	.011	.022	.035	.061	.095	.139	.175	.230	.283	.317	.847	.283	.213	.166	.098	.061	.025
-25				.058	.078						.362	.342					
-30	.011	.020	.030	.050	.075	.110	.142	.190	.244	.280	.293	.665	.254	.205	.128	.085	.032
-35					.073							.343	.317				
-40	.014	.028	.028	.042	.059	.080	.106	.145	.202	.221	.242	.290	.589	.270	.164	.115	.046
-45													.326	.345			
-50	.023	.034	.034	.043	.050	.062	.075	.108	.155	.183	.208	.250	.285	.486	.218	.156	.065
-55														.369	.291		
-60	.044	.054	.045	.049	.046	.052	.060	.077	.115	.147	.175	.224	.267	.324	.413	.224	.098
-65								.074							.334	.304	
-70	.098	.115	.074	.063	.049	.047	.045	.062	.091	.109	.146	.190	.226	.296	.300	.385	.159
-75																.364	.236
-80													.203			.339	.349
-85																	.344

TABLE II

LUNAR MODEL
NONCOPLANAR PHOTOMETRIC FUNCTION
(a = 90°)

SENSOR ANGLE (DEG)	SOURCE ANGLES (DEG)																
	80	70	60	50	40	30	20	10	0	-10	-20	-30	-40	-50	-60	-70	-80
65		.063	.076		.122	.127	.101	.106	.098	.106	.101	.127	.122		.076	.063	
60	.035	.061	.078	.132	.132	.107	.110	.111	.119	.111	.110	.107	.132	.132	.078	.061	.035
50	.032	.054	.076	.131	.136	.123	.133	.133	.152	.133	.133	.123	.136	.131	.076	.054	.032
40	.028	.051	.072	.130	.147	.143	.157	.169	.194	.169	.157	.143	.147	.130	.072	.051	.028
30	.025	.047	.071	.137	.160	.166	.189	.201	.240	.201	.189	.166	.160	.117	.071	.047	.025
20	.023	.045	.071	.143	.172	.181	.227	.241	.291	.241	.227	.181	.172	.143	.071	.045	.023
10	.025	.045	.071	.143	.183	.200	.239	.272	.357	.272	.239	.200	.183	.143	.071	.045	.025
5	.024	.044	.070	.147	.184	.201	.242	.293	.429	.293	.242	.201	.184	.147	.070	.044	.024
0	.024	.044	.071	.145	.190	.210	.250	.300	1.000	.300	.250	.210	.190	.145	.071	.044	.024
-5	.023	.046	.071	.144	.184	.207	.247	.293	.432	.293	.247	.207	.184	.144	.071	.046	.023
-10	.023	.045	.071	.143	.183	.199	.238	.275	.359	.275	.238	.199	.183	.143	.071	.045	.023
-20	.025	.047	.072	.144	.175	.196	.220	.245	.283	.245	.220	.196	.175	.144	.072	.047	.025
-30	.026	.048	.076	.141	.163	.169	.196	.214	.244	.214	.196	.169	.163	.141	.076	.048	.026
-40	.029	.052	.080	.136	.150	.145	.155	.174	.202	.174	.155	.145	.150	.136	.080	.052	.029
-50	.032	.055	.080	.129	.136	.124	.132	.129	.155	.129	.132	.124	.136	.129	.080	.055	.032
-60	.036	.062	.083	.130	.124	.108	.111	.110	.115	.110	.111	.108	.124	.130	.083	.062	.036
-65		.065	.092		.118	.102	.098				.098	.102	.118		.092	.065	

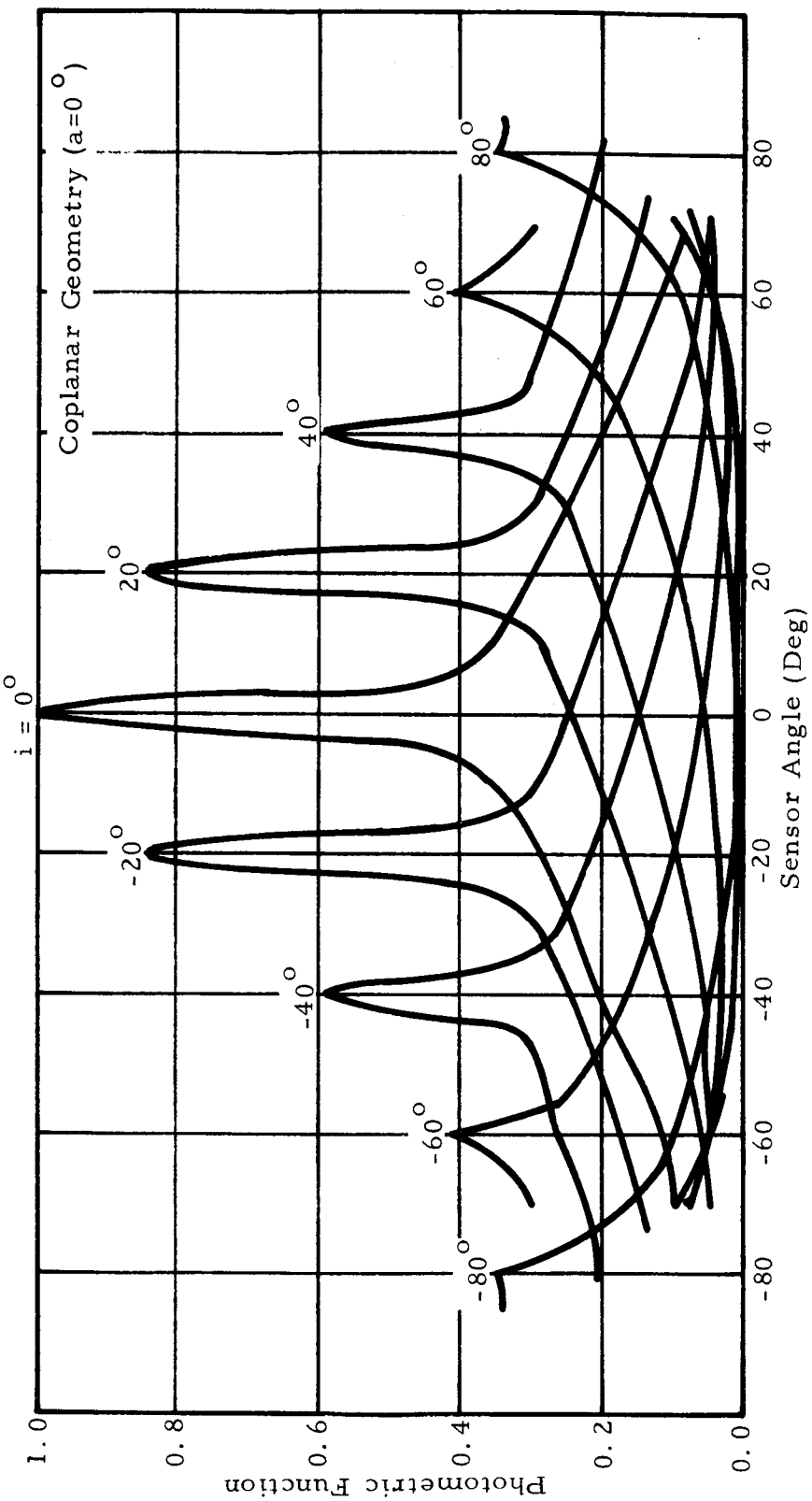

Figure 9 Lunar Model Photometric Calibration

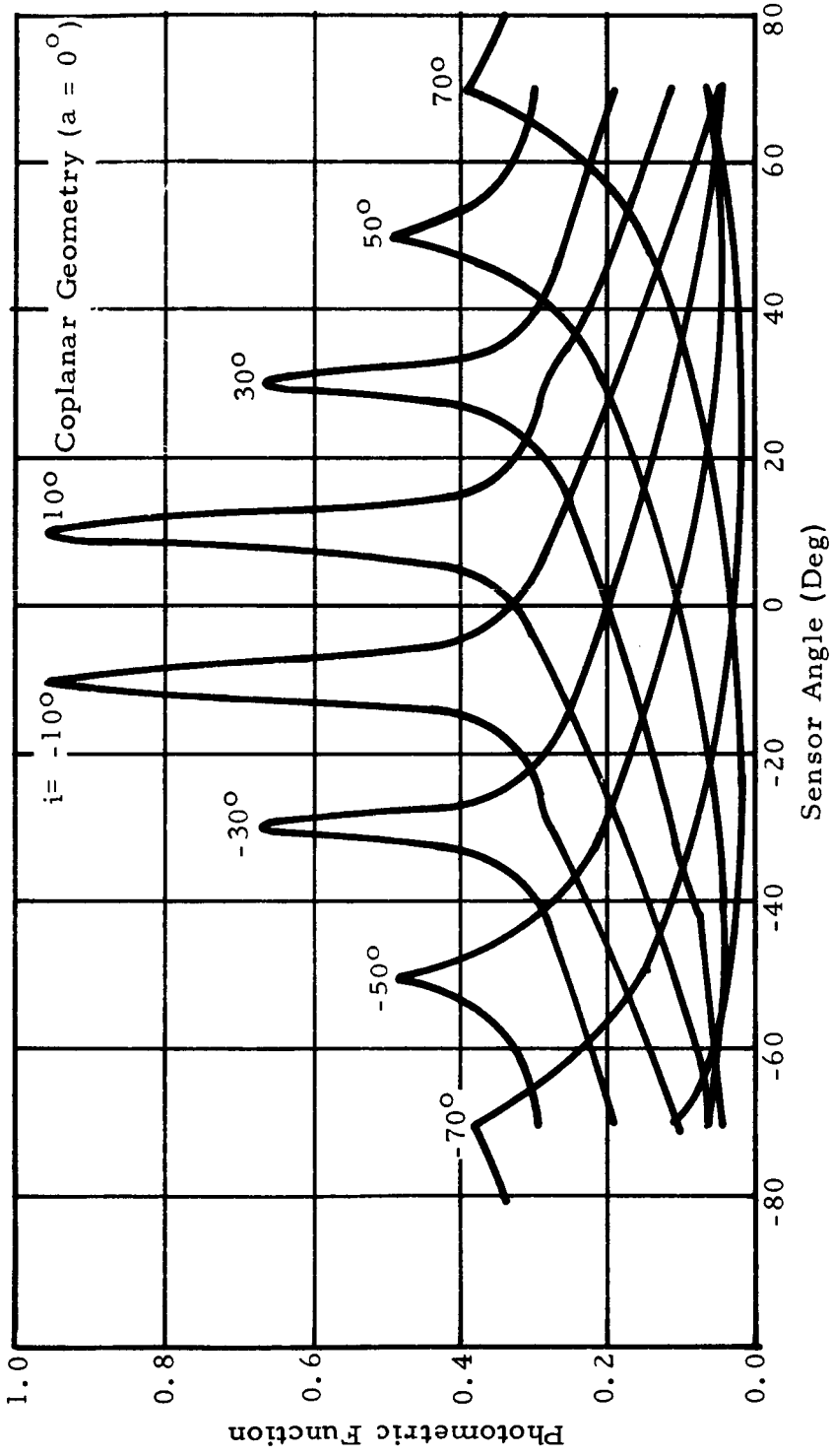

Figure 10 Lunar Model Photometric Calibration

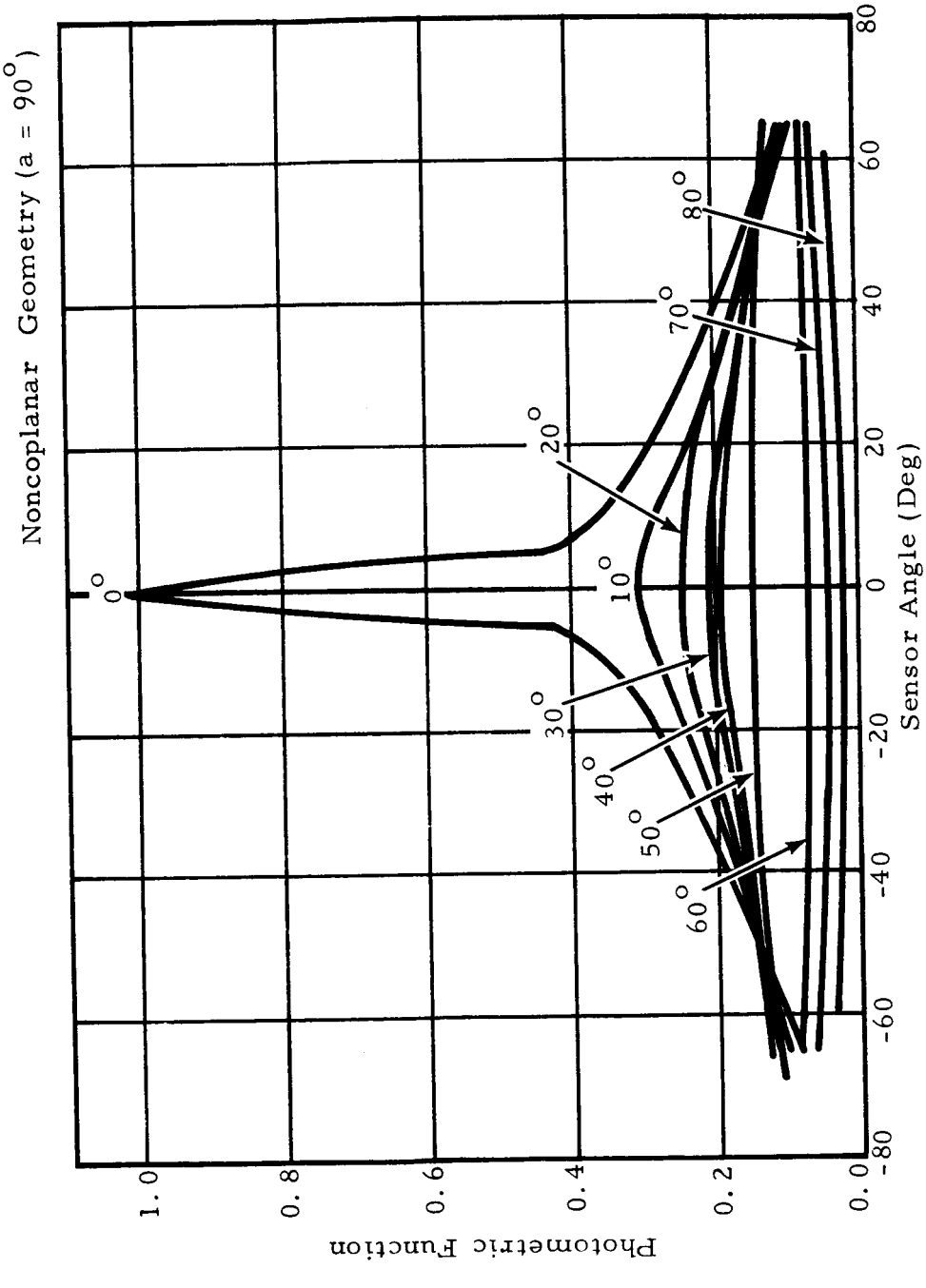

Figure 11 Lunar Model Photometric Calibration

This defect cannot be corrected without using a radically different photometric material, where the porous layer itself is the strong reflector, just as the case for the lunar surface. But as long as the model is accurately calibrated, it is possible to use it just as if it reproduced the moon's properties exactly. The methods and procedures will be unaffected.

It is probable that this difference will not produce significantly different relative luminance values in a photograph than would be obtained for a lunar photograph. The reason is that the range of surface slopes is usually quite small, 30° being large for a maria region. Therefore, the range of apparent source angles, which for any region of maria is equal to the range of slope angles, will be small. This means that the set of photometric curves which apply to a given photograph will only cover some 30° in source angle, and by examining Figures 9, 10, and 11, for high and low source angle, ($i > 50^{\circ}$ or $<30^{\circ}$), the peak values do not change very much over 30°. So for these geometries, high and low source angles, the reflectance peaks do not vary too much more than the lunar values do, which should reduce the differences in appearance that might result. The obsolete values of the luminances will, of course, be smaller.

The second major difference is that the reflectance peaks are much sharper on the lunar model than for the lunar functions (Herriman et al., 1963). The theoretical photometric function of Hapke (1963) can be used to quantify this difference. His back-scattering function, $B(\alpha, g)$ was dependent on a compaction parameter g which had a range of 0.4 to 0.8 for typical lunar regions. A value of $g = 0.6$ produced curves which best matched the JPL near-lunar photometric function. The value of the Hapke parameter which best matched the curves for the lunar model was 0.2, indicating a much sharper peak than is observed for the lunar surface. The only way to correct this defect would be to use a larger pore size for the photomat, but this would cause an increased albedo and a less pronounced back-scatter, and both these effects would have to be balanced against the advantages of decreasing the sharpness of the peak.

Two other factors which should be noted are the fall of the curves for $|\epsilon| > |i|$ and the forward scatter at high sensor angles. For the geometry "source below sensor at high source angles" or $|\epsilon| > |i|$ for $|i| \geq 60^{\circ}$, the photometric function falls off much more slowly than the JPL curves. This is due to an isotropic scattering component from the upper layers of the blackened foam surface, which becomes more important relative to the strong substrate return as the source angle becomes large and the ratio of foam surface to substrate surface increases. There is no practical way to improve this. The forward scattering component, which

for $i \leq 60^{o}$ is fairly similar to the forward scatter observed for the moon, becomes very large for $i > 60^{o}$. This is also due to reflectance from the foam surface, and prevents the model from being used accurately for geometries where the camera line of sight is within 20^{o} of the surface, pointtin toward the sun.

One problem encountered in the early phase of the calibration program was an unevenness or lumpiness in the photometric curves. Small humps would appear at different values of i for different sensor angles. The cause of this was found to be the resolution of individual "anomalous" pores in the photomat material. The early photometric readings were obtained with the sensor at a 1. 5m range. Due to the mechanical swirling process which is used to aerate the plastic, there are regions in the Scott foam sheets which have oversize or undersize pores. The average pore density is 0. 8 pores/mm, but some pore regions can have pores 2 to 3 times this large, or much smaller. If an area containing a group of undersize or oversize pores are centered in the photometer field of view, the resultant curves contain local humps where large areas of the substrate show through. The only solution to this is to place the sensor at a range which is sufficient to ensure that the field of view covers a large number of pores. For the sensor used in this experiment, a minimum range of 3. 0m was required. Even at this range, a visual inspection through the photometer telescope had to be made for each area to ensure that no very large or very small pores were in the field of view. If this care is not taken, not only will unevenness in the photometric curves result, but the resultant photometric function will be different due to the much more open or dense pore structure.

The second set of photometric functions, the noncoplanar ($a = 90^{o}$) geometry, cannot be compared to the lunar case, since this geometry is only attainable by a satellite in a lunar polar orbit. These data, in fact, represent the first attempt at constructing a photometric function for a lunar-type surface for this satellite geometry. In theory, the photometric functions for any satellite orbit with inclinations from 0^{o} (the coplanar geometry) up to 90^{o} (polar) can be generated by interpolation between these two sets. Due to the rather large differences in their forms, however, this a difficult practical problem (see next section).

The general characteristic of the $a = 90^{o}$ geometry is that for small source angles (near 0^{o}) the photometric function is quite close to the coplanar case. But as the source angle increases, the luminance at all sensor angles drops, and the peak is always at 0^{o} sensor angle, independent

of the source angle. Finally for source angles $i \geq 50^{\circ}$, the reflectance is almost completely independent of sensor angle, but still strongly dependent on source angle (for example, the reflectances at $i = 80^{\circ}$ are less than one-third of those for $i = 60^{\circ}$). In the next section these curves are discussed in more detail.

One interesting comparison may be made which lends credance to photometric function for the noncoplanar geometry. Although there are no other experimental data to compare with these curves, there is an analytical comparison which can be made. The theoretical photometric function derived by Hapke, which has been demonstrated to match closely with the lunar photometric data, is capable of generating photometric functions for any geometry. A theoretical photometric function has been computed for the $a = 90^{\circ}$ geometry using the Hapke equation, with a compaction parameter of 0.6. The resultant curves are shown in Figure 15, and the qualitative agreement with the lunar model curves is striking. All the pertinent characteristics agree; the shape, the i and ϵ dependence are quite similar. The peak is much broader for the Hapke curves, but this is due to the lunar value of the compaction parameter. Also the values for the very high source angles are much lower than the values for the lunar model, but this is probably due to the isotropic scattering from the foam surface. This agreement provides strong support for the validity of the noncoplanar photometric function.

D. Albedo Calibration

The same instrumentation and general procedures were used to measure the mean normal albedos of the lunar model. Since this measurement has to be made at $i = \epsilon = 0^{\circ}$, the beam splitter technique was used. Early laboratory studies showed that measuring the luminance at small source angles ($\epsilon \approx 1^{\circ}$) produced significant errors in the resultant extrapolation to the peak ($\epsilon = 0^{\circ}$), due to the very rapid change in the photometric function near $i = \epsilon = 0^{\circ}$ (See Figure 9).

The normal albedo is defined as the ratio of the luminance of the model at $i = \epsilon = 0^{\circ}$ to the luminance of the magnesium oxide reflectance standard. The mean absolute reflectance of the magnesium oxide block was estimated as 0.98, and it was found to be lambertian for all angles up to 60° from the normal to the surface. The procedure was first to position the model in the target beam and measure the total luminance. Then the magnesium oxide block was placed in the target beam and the total

luminance measured. The sink and beam splitter luminances were then measured and subtracted from the two totals. The ratio of the resultant luminances gives the mean normal albedo of the model with respect to the reflectance standard.

It was also necessary in this experiment to be very careful of the model pore structure. A minimum sensor distance of 3.0m and visual inspection of the surface were always required to ensure no anomalous pore areas.

The results of the albedo calibration are given in Table III. The mean-normal albedo of the lunar model, as measured for five areas, is 0.0515, or 5.15%. The albedo of the witness model, measured for three areas, was found to be 4.88%, slightly lower than lunar model average. The albedo variance areas, provided in the form of four areas as shown in Figure 6, were also calibrated in the same manner. The albedos of this set of areas ranged from 0.072 to 0.079, as tabulated in Table III.

TABLE III

LUNAR MODEL NORMAL ALBEDO VALUES

Location	Mean Normal Albedo	RMS Deviation
Lunar Model	0.0515	0.0056
Witness Model	0.0488	0.0031
Albedo Variances*		
Area 1	0.0720	0.0042
Area 2	0.0784	0.0018
Area 3	0.0794	0.0015
Area 4	0.0784	0.0018

*Refers to areas on the model designated in Figure 6.

V. PHOTOMETRIC AND PHOTOGRAMMETRIC ANALYSIS

A. Photogrammetric Studies of the Lunar Model

The photogrammetry experiment was designed to provide information concerning the accuracy and repeatability of photogrammetric measurements on lunar-type surface. The base-to-height ratio chosen for this experiment was equal to that of the Lunar Orbiter, 0.388. The resolution of the optical system was adjusted so that features eight times as large as those at the resolution limit of the high-resolution camera system would be just recognizable. This gave a minimum recognition size of 8 times 12 mm or 9.6 cm.

A series of stereo photographs was obtained with a variety of sun-camera geometries, using the specified base-to-height ratio and resolution. The lunar model was illuminated by the sun, and the camera system placed 19 m from the model. The theodolite and steel tape were used to position the various components accurately. Once taken, the photographs were all developed in a uniform manner, so that no processing effects would enter.

The nine areas chosen on the lunar model for photogrammetric measurement included two small eroded craters, a small and a moderate size dome, a moderate and a large crater, a wrinkle ridge peak, two locations in the large rill, and a calibrated slope area. These areas were chosen to provide a wide range of surface characteristics, and a range of sizes, from just below to much larger than the resolution limit.

The photogrammetric reduction was carried out trigonometrically using the standard equations for the problem. The height above the reference point was 19 m; the stereo baseline was 7.1 m and the film image format was 10.2 cm x 12.7 cm. The results of these measurements are given in Table IV for six photographs and nine model areas for the x and y coordinates. The true coordinates (mm) taken from the contour map are given for each of the six photographs. In the columns labelled "Mean Coordinates," the mean values of four areas are tabulated, for photographs 1, 2, 3, 5 and 6. In the last two columns, the ratio of the mean error to the mean coordinate is given, which is a measure of the fractional error in the experiment.

The results for photographs 1 and 2 are in general the best. This corresponds to camera nearly overhead and the sun at 45°. The results for

TABLE IV

PHOTOGRAMMETRIC MEASUREMENTS

Model Area	True Coordinates* (mm)		Photograph 1		2		3		4		5		6		Mean Coordinate (mm)		Mean Error	
	x	y	x	y	x	y	x	y	x	y	x	y	x	y	x	y	x/x	y/y
1	871.73	1542.29	1133.86	1505.71					365.76	1167.38								
2	1033.27	559.30	978.41	448.06	990.60	481.58	691.90	597.40	408.43	469.39	929.64	496.82	804.67	384.05	887.82	481.58	-0.144	-0.136
3	1917.19	865.63	2130.55	810.77	1941.58	832.10			877.82	688.85	2176.27	856.49	1804.42	734.57	2011.68	807.72	+0.049	-0.067
4	1741.63	1361.39					1572.77	960.12										
5	2694.43	246.89	3066.29	384.05														
6	3406.14	2308.86	3770.38	2417.06														
7	2877.31	2121.40	3066.29	2133.60	2685.29	1905.00	2097.02	2020.83	1161.28	1520.95	3093.72	2093.98	2764.54	1850.14	2740.15	1999.49	-0.048	-0.057
8	1313.99	237.74	1344.17	3508.24			890.02	2965.70										
9	670.56	2212.85	731.52	2316.48	734.57	2301.24	621.24	2142.74	310.90	1691.64	731.52	2453.64	384.05	2200.66	640.08	2282.95	-0.045	+0.032

*Refer to Figure 5 for location on model

photographs 3 and 4 are considerably worse, the photograph 4 results being extremely in error. Here the sun is again at 45° to the normal, but the camera is 30° and 50° (approximately) to the normal, the latter being a very high oblique shot. The results for 5 and 6 are not as good as 1 and 2, but are not too bad. This geometry was a high sun angle, 60° to normal, with the camera nearly overhead. The mean values and diviations are computed neglecting photograph 4 where $\epsilon \approx 50^{\circ}$, since the high oblique view has introduced large errors not attributable to the model structure. In general, the results shown in the table indicate a fair degree of repeatability, and a mean error of the order of 5 to 10%. This is considered to be an upper limit: for reasons explained below.

Experimental difficulties in the photogrammetric experiment produced a number of undesirable features which are related. The large number of unmeasured coordinates shown in the table, the moderate-to-large errors, and the absence of the z-coordinate measurements are all the result of the two causes. The first cause is that use of photogrammetric methods to measure positions under the combined circumstances of very uniform surface appearance, low resolution and unfavorable source-sensor geometry produces considerable errors. Thus only at moderate to low sensor angles and high source angles is the geometry favorable to making accurate measurements. Further, the low resolution limits severely the size of the feature which can be accurately measured. Even features which are resolved may be too indistinct or blurred to permit accurate location of reference points. The second cause of error in this set of measures is inadequacy of the lunar photometric model for photogrammetric measurements. Initially the model was designed to be used at high resolution for photometric studies, the minimum feature size being 12 mm. This required a fair number of small features, and the lunar topographic requirement that the number of features (craters) of a given size is inversely proportional to their diameter meant that only a few large objects could be represented. This, combined with the size limitations of the model itself, meant that only a few features on the lunar model have a size which can be resolved by the very low resolution required for the experiment. In other words, the resolution element of 9.6 cm is so large relative to the model features that only a very few could be recognized or discerned under the best viewing conditions.

This problem is better appreciated by seeing Figure 12, which shows the lunar model as it appears at the resolution required for the photogrammetric experiment Only the large rills and the section of the large crater at the upper right are discernible. All the other features are lost, and when this characteristic is combined with a source-sensor geometry where contrast between features is suppressed, such as in Figure 13 where the sun is almost at the zenith, the low-resolution photogrammetry can only be applied to very large features.

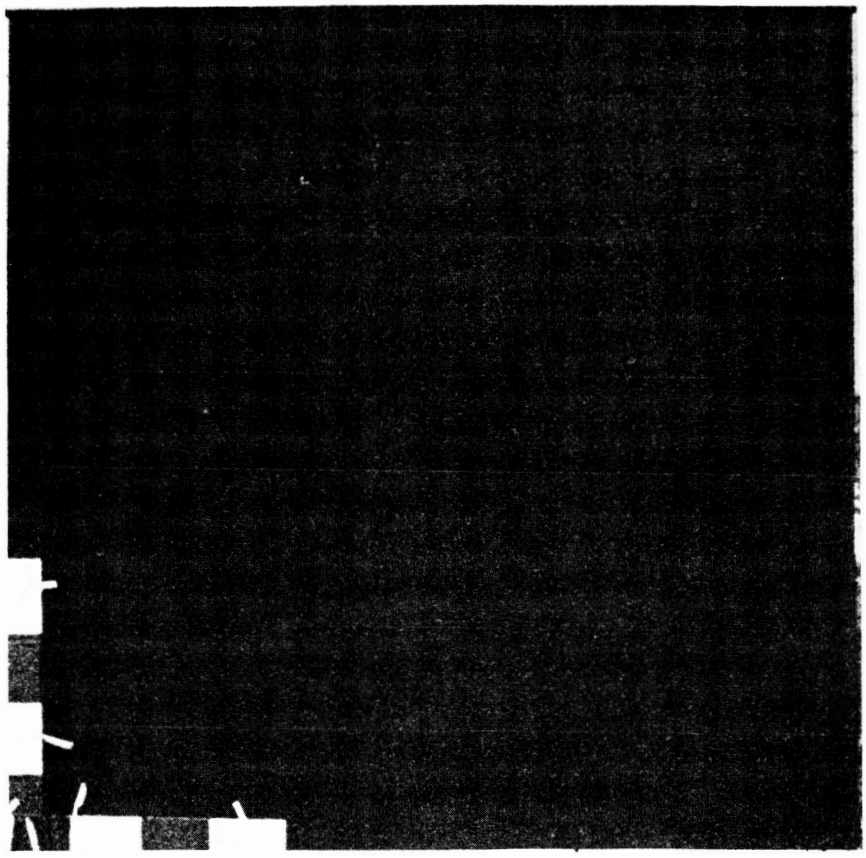

Figure 12 Appearance of Lunar Model at Low Resolution Required for Photogrammetric Analysis

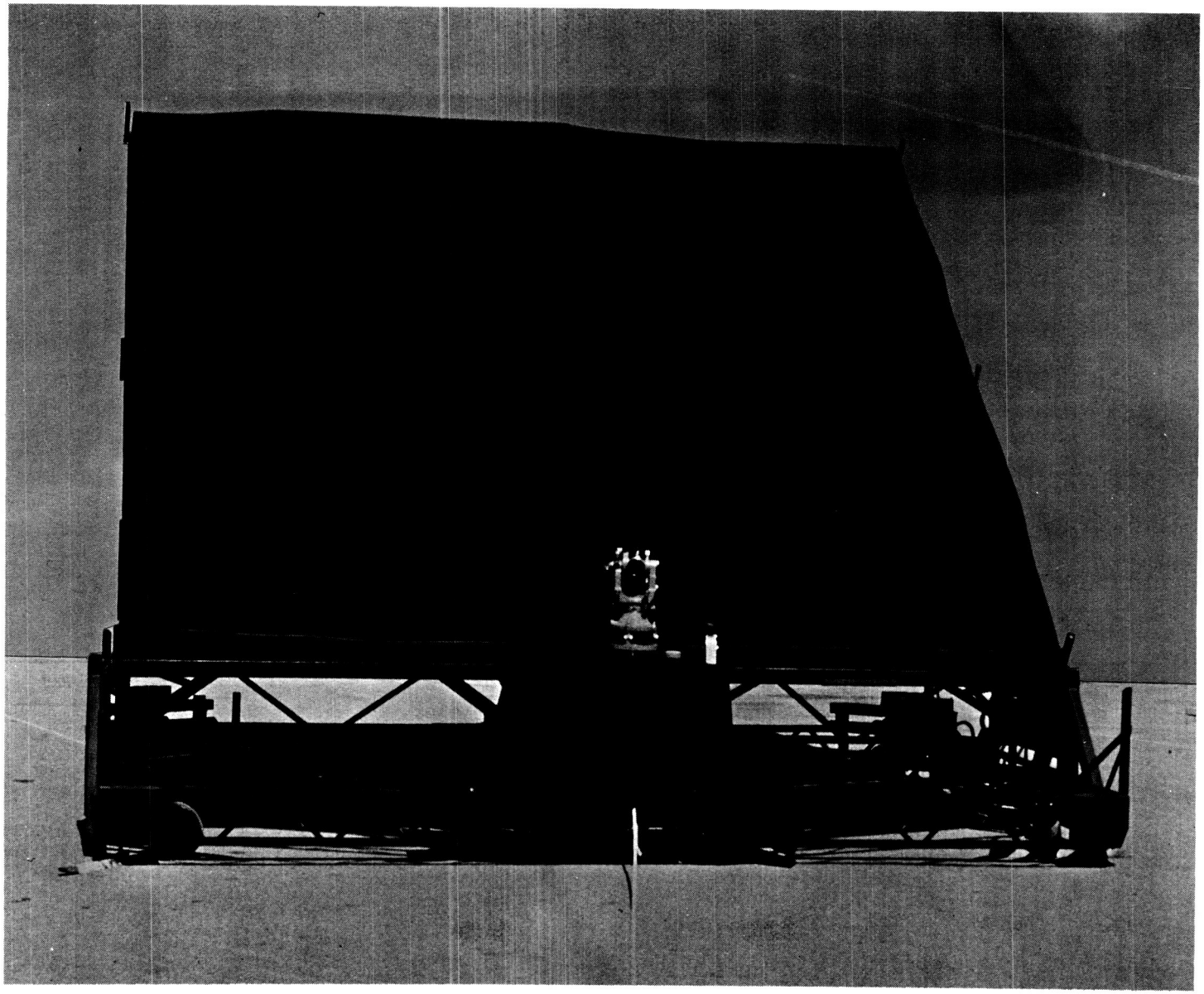

Figure 13 Appearance of Lunar Model for Low Source Angle ($i = 9^{o}$)
Photometric Experiment

This is the reason that many of the features tabulated in Table IV have x, y coordinates measured only for a few cases. The features are not recognizable at most source angles; therefore, an accurate estimate of their position is impossible. This factor is also responsible for the large errors, where they do occur. The worst error produced was the complete inability to measure z coordinates, the heights of features. The very gradual luminance gradients, and the lack of any texture or points which could be used to focus on, produced a "floating image." Even for those few large features that could be recognized, the lack of any sharp or clearly defined feature made it impossible to focus the stereoscope and obtain a parallax. The problems encountered in this experiment give some indication of the difficulty to be expected in trying to correlate the high resolution and the low resolution Orbiter data.

The results of this section may be summarized as follows:

1. Where the model features could be resolved, low-resolution photogrammetric measurements could be made repeatable, and with an error of 5 to 10%. This is an upper limit to the error: under real lunar conditions, the equivalent system should produce considerably better results.

2. Only those features which are several times the resolution element in size, and which have moderate luminance gradients, can be reliably measured. The very gradual luminance gradients present under most lunar surface experiment geometries would make it quite difficult to retain high accuracy.

3. Observations taken with greatly exaggerated geometry (high obliques) are much more affected by the effects producing errors. Thus high sensor angles should be avoided.

4. All low-resolution photogrammetry should be performed at as high a sun angle as possible (sun near horizon). Low sun angles (sun near zenith) will allow only measurement of very large features. Sun angles $i > 70^{\circ}$ are the best for photogrammetry, and for $i < 70^{\circ}$. Many features lack the distinctness and sharpness acquired for accurate measurement.

B. Photometric Studies of the Lunar Model

The photometric function of the lunar model, as illustrated in Figures 9, 10, and 11, provides a tool for analyzing the photometric technigues to be used in the lunar program. From the figures, it can be seen that the lunar model photometric function is strongly dependent on the three angles which define the geometry, i, ϵ and a (or α). For the coplanar geometry ($a = 0^{\circ}$) and for small values of a, the function is quite

strongly differentiated in both i and ϵ ; i.e., the individual curves are well separated. For the a = 90° case and for all large values of a, the function is even more strongly differentiated in i, but it is very weakly dependent on ϵ at all but the smallest source angles. This means that the apparent luminance of a surface will change only slightly when viewed from different sensor angles, but will change greatly for different source positions.

The accuracy and repeatability of the photometric function depend on the inherent accuracy of the photometry, angular measurements, and systemetic errors in the calibration procedure. The photometer accuracy is only reported as 5%, but seems to be considerably better than this. The angular measurements are accurate to better than 1%. The mean deviations of the individual photometric functions from the mean function are approximately ± 0.03 for large source angles (i > 40°), and approximately ± 0.05 for small source angles (i < 40°). The estimated mean error in the JPL mean lunar photometric function is ± 0.02 (Parker et al., 1964), which is slightly better than the values obtained in this study. The increase in scatter for small source angles is easily explained: for small source angles, the pore structure is viewed almost perpendicularly, so that any anomolous pore structure is emphasized. As the source angle becomes large, the light path through the foam layer becomes longer, and a larger pore volume influences the reflected return, which minimizes the effects produced by a few over- or under-size pores in the center of the illuminated field. If the explanation is correct, the increase in the errors at small i means that the effects of pore irregularities were not entirely eliminated by the experimental procedure. It also indicates that the mean error ± 0.03 is a probable minimum value for the present model: this much variation is a characteristic of the model.

A direct comparison of the lunar model photometric function to the JPL mean lunar function (Willingham, 1964) shows the fall-off of the lunar with increasing source angle, the much sharper peaks, and lower values at all values of ϵ for any i. The theoretical photometric function derived by Hapke (1963, 1966) to represent the lunar surface has been shown to match the lunar data and the JPL function fairly well. This theoretical photometric function is given in Figure 14 for a = 0°, 70°, and 90°; and for i = 0°, -40°, and -80°. The same general character is present for the 0° and 90° geometries as is observed for the lunar model. The major disagreements have been discussed above.

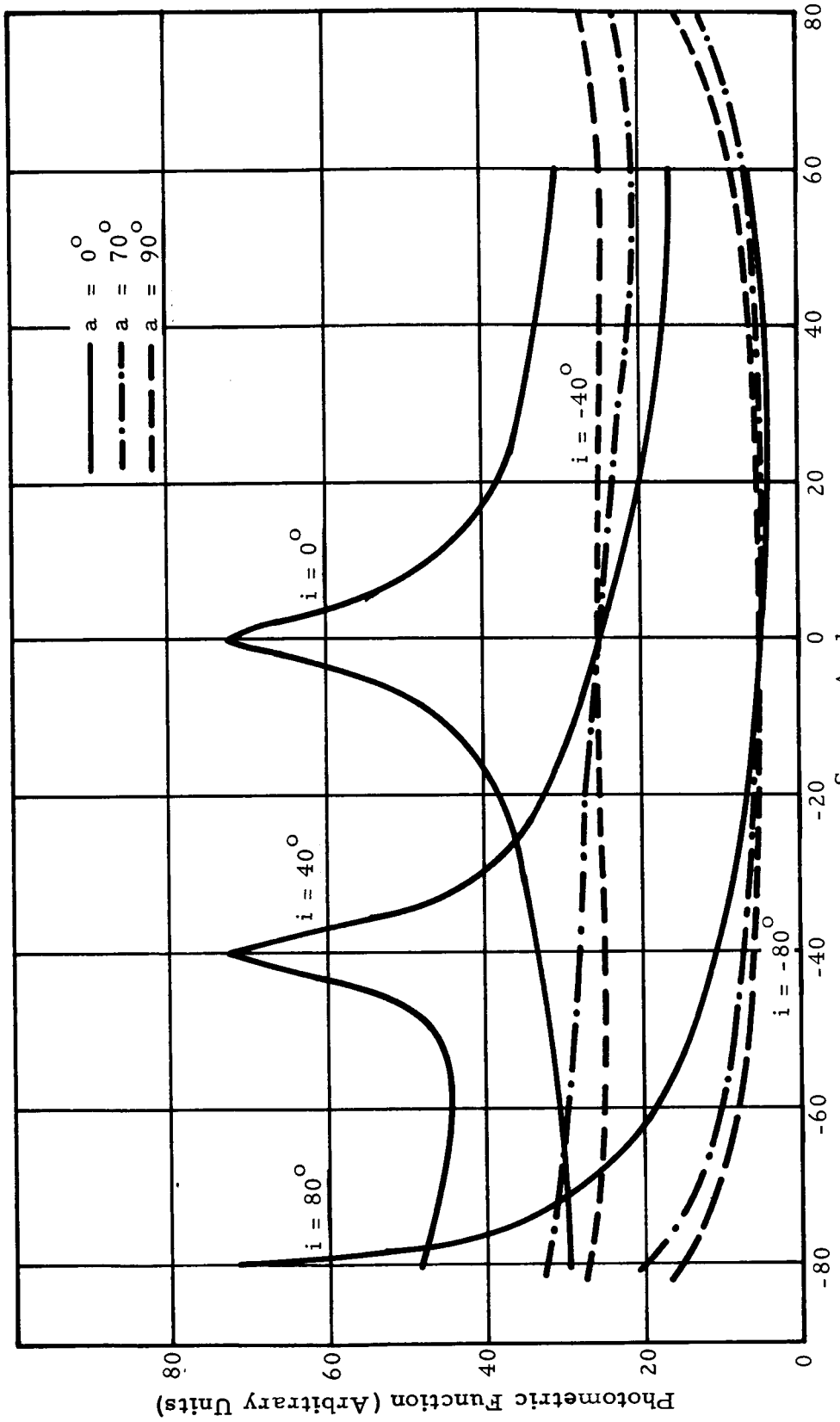

Figure 14 Theoretical Photometric Function for a = 0°, 70°, 90°

An analytical equation which closely matches the lunar model photometric function can be obtained by modifying the Hapke function. The Hapke equation is of the form:

$$B = E_o \, r \, \frac{1}{\pi} \, \Phi_o \, (i, \epsilon, \alpha)$$

where:

B = the target luminance in candles/cm^2

E_o = illuminance in lumens/cm^2

r = normal albedo

Φ_o = Hapke theoretical photometric function

α = the phase angle which is a function of i, ϵ, and a.

$$\Phi_o \, (i, \epsilon, \alpha) = \frac{1}{1 + \frac{\cos \epsilon}{\cos i}} \left[\frac{\sin \alpha + (\pi \alpha) \cos \alpha)}{\pi} + 0.1 \, (1 - \cos \alpha)^2 \right] B(\alpha, g)$$

where g is the compaction parameter indicating the degree of porosity of the material, and

$$B \, (\alpha, \, g) = \begin{cases} 1 & \alpha \geq \pi/2 \\ 2 - \frac{\tan \alpha}{2 g} \left(1 - e^{-\frac{g}{\tan \alpha}}\right)\left(3 - e^{-\frac{g}{\tan \alpha}}\right) & \alpha < \pi/2 \end{cases}$$

This equation was used to compute the photometric function given in Figures 14 and 15.

Now, if a multiplier is added of the form

$$A_1 = (0.37 + 0.63 \cos^4 i)$$

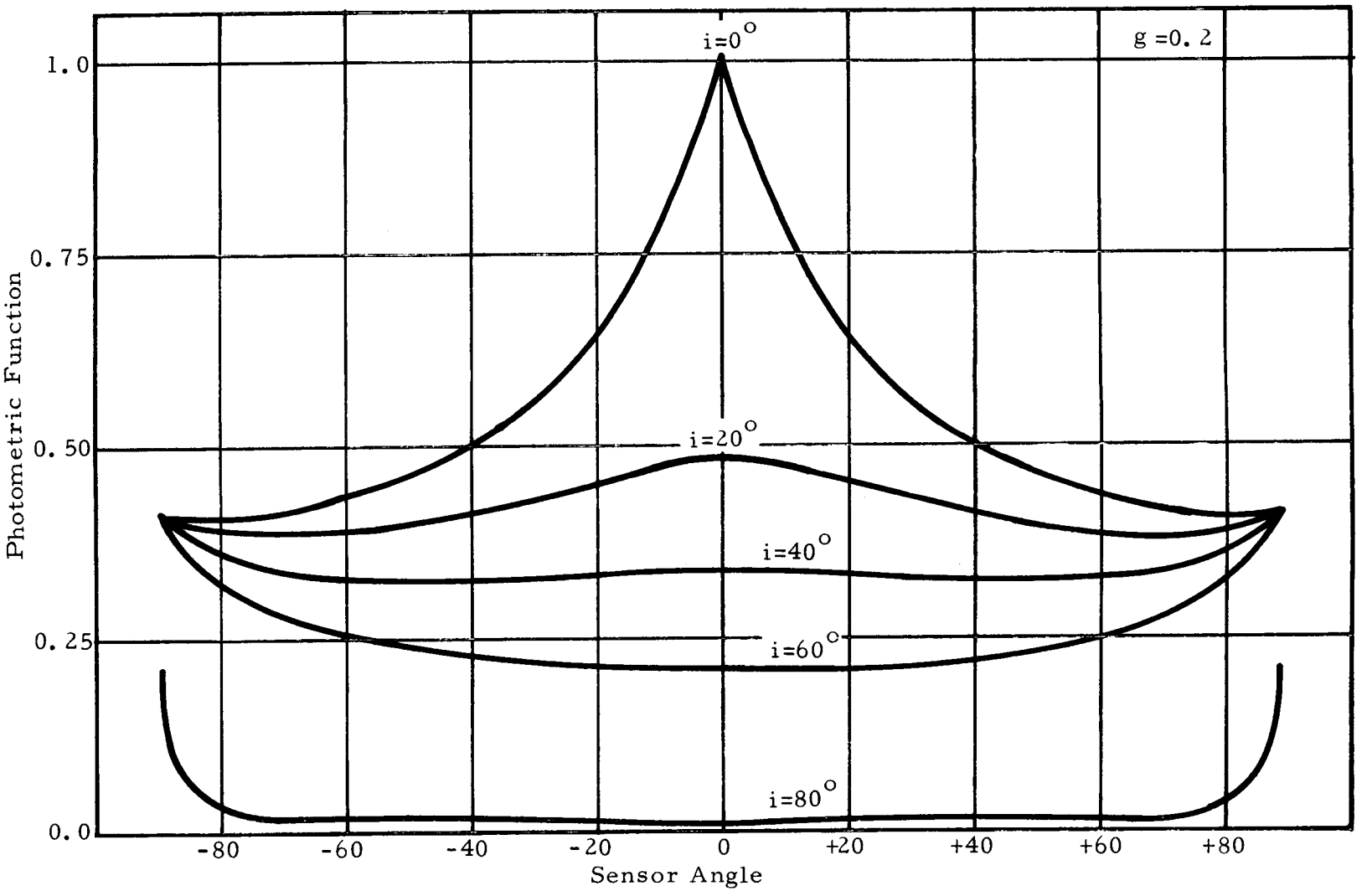

Figure 15 Hapke Theoretical Lunar Photometric Function for Noncoplanar Geometry (a = 90°)

the resultant photometric function has a envelope of peak reflectance very close to that of the lunar model. A second term,

$$A_2 = (1 - \cos^2 i \sin |i - \epsilon|)$$

is needed to reduce the value of B for sensor angles away from the region $i = \epsilon$, for low source angles. The modified theoretical function is defined as

$$\Phi = A_1 A_2 \Phi_o .$$

Computing this for $a = 0^o$ coplanar geometry, the resultant photometric function is compared to the lunar model measured values in Figure 16. The agreement is reasonable and indicates that the equation given above can be used to perform analytical studies.

It is necessary, in the next section, to utilize a photometric function for a geometry where the angle a lies between the calibration values of 0^o and 90^o. Since there are no calibration data available for intermediate values of a, an empirical photometric function must be generated by interpolation between the measured sets. A brief examination of the photometric curves makes it clear that a simple interpolation procedure would be very inaccurate. The entire character of the photometric curve changes radically between $a = 0^o$ and $a = 90^o$. Having only this information with which to proceed, it is almost impossible to obtain reliable results; if the theoretical photometric function is utilized, a much more accurate procedure can be developed.

It has been found that the theoretical photometric function matches the JPL function fairly well (Hapke, 1963). Further, it can be modified to represent the lunar model function by the inclusion of two modifying terms. The method devised for generating the lunar model photometric function for $0^o < a < 90^o$ uses the theoretical photometrical function to compute a scale factor, or interpolation factor, which is used to transform $a = 0^o$ curves into $a > 0^o$ curves or $a = 90^o$ curves into $a < 90^o$ curves. This interpolation factor computed for the theoretical photometric function is then used to compute an empirical photometric function for $0^o < a < 90^o$ for the lunar model.

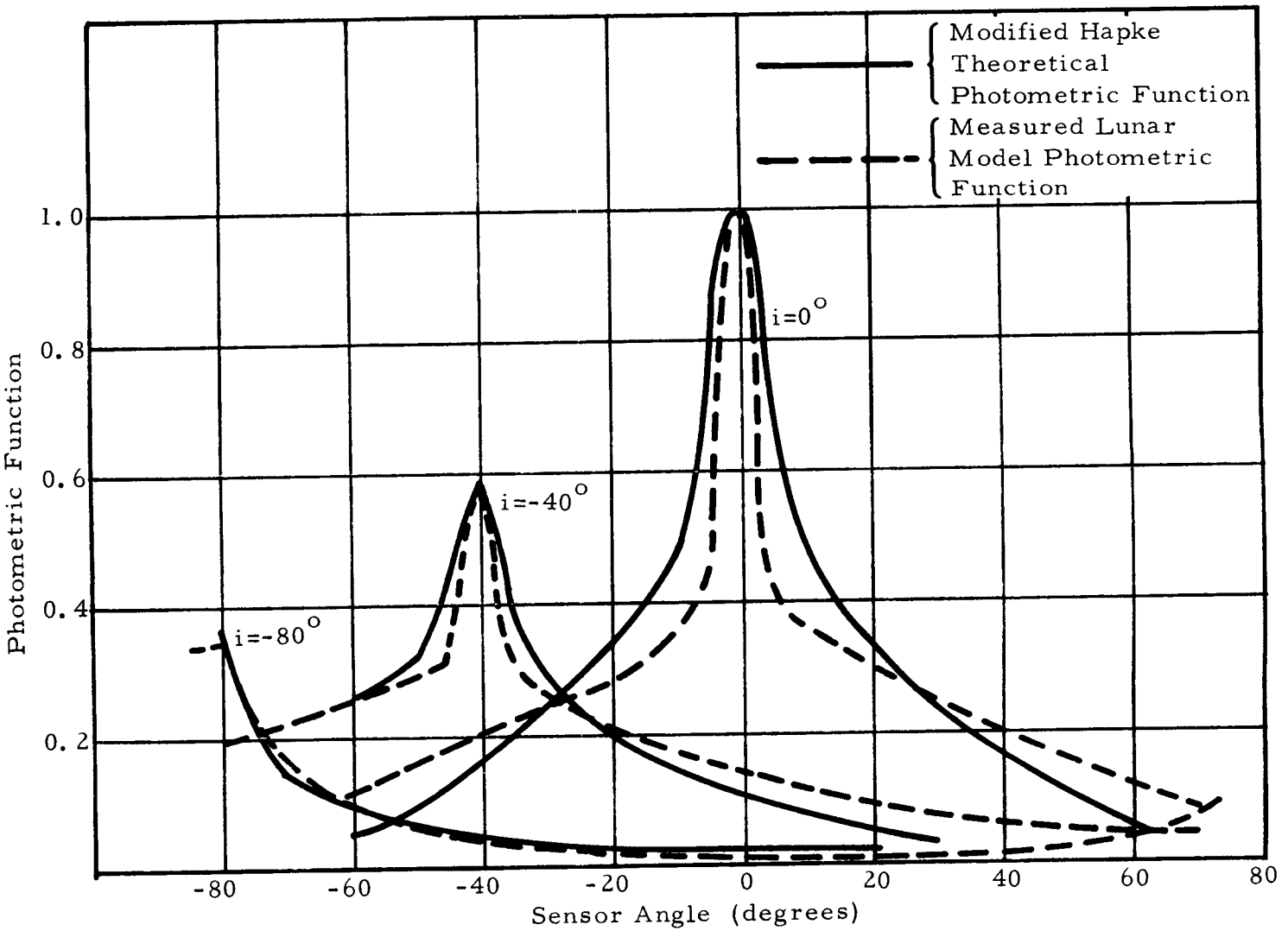

Figure 16 Comparison of the Lunar Model Photometric Function With a Modified Hapke Theoretical Photometric Function

This procedure was carried out for the noncoplanar geometry $a = 70^{\circ}$, which is the geometry used in the photometry experiment described in the next subsection. The results are shown in Figure 17, where the lunar model empirical photometric function for $a = 70^{\circ}$ is given, for negative source angles. The functions for positive source angles are similar in shape, but are asymmetric in the opposite direction, toward positive sensor angles. Figure 14 shows that the theoretical photometric curves for $a = 70^{\circ}$ are very similar to those for $a = 90^{\circ}$, being slightly asymmetrical with respect to $\epsilon = 0^{\circ}$. This causes the $a = 70^{\circ}$ curves to be quite similar to the measured $a = 90^{\circ}$ curves, yet having a marked asymmetry in the direction where $i = \epsilon$. This empirical function is used in the next section to perform photometric slope and albedo measurements. It is possible by the same process to calculate a photometric function of this type for any value of a in the range 0° to 9°. In practice, it would be much better to measure the photometric function for $a = 45^{\circ}$, thus providing a central set of values and allowing a better interpolation to be made.

C. Slope and Albedo Determination by the Photometric Method

The photometric method of determining albedos and surface orientation for lunar-type surfaces is based upon the unique nature of the lunar photometric function. Albedo measurement is equally feasible for any type of surface, but for most materials the angular dependence of reflectance does not allow any estimate of surface orientation.

For a given surface element, the luminance is given by

$$B = E_o \, r \, \phi (i, \epsilon, \alpha)$$

so that if E_o and ϕ are known, a measurement of B yields the normal albedo, r, directly. For a lambertian surface, $\Phi = 1$ so the ratio of the luminance to the illuminance gives the normal albedo. The same principle can be applied to a strong back-scatterer such as the lunar model, but Φ now can assume quite different values, dependent on i, ϵ, and α.

In general, the albedo acts as a uniform scale factor: any changes in luminance are scaled on the same ratio for all values of i, ϵ, and α. Changes in the geometry, however, cause significant shape changes in the resultant luminance curves, since the photometric function is responsible for this effect. In theory, it is possible to determine both albedo and surface slope directly from one set of photometric measurements (at least two measurements are required with one of the three

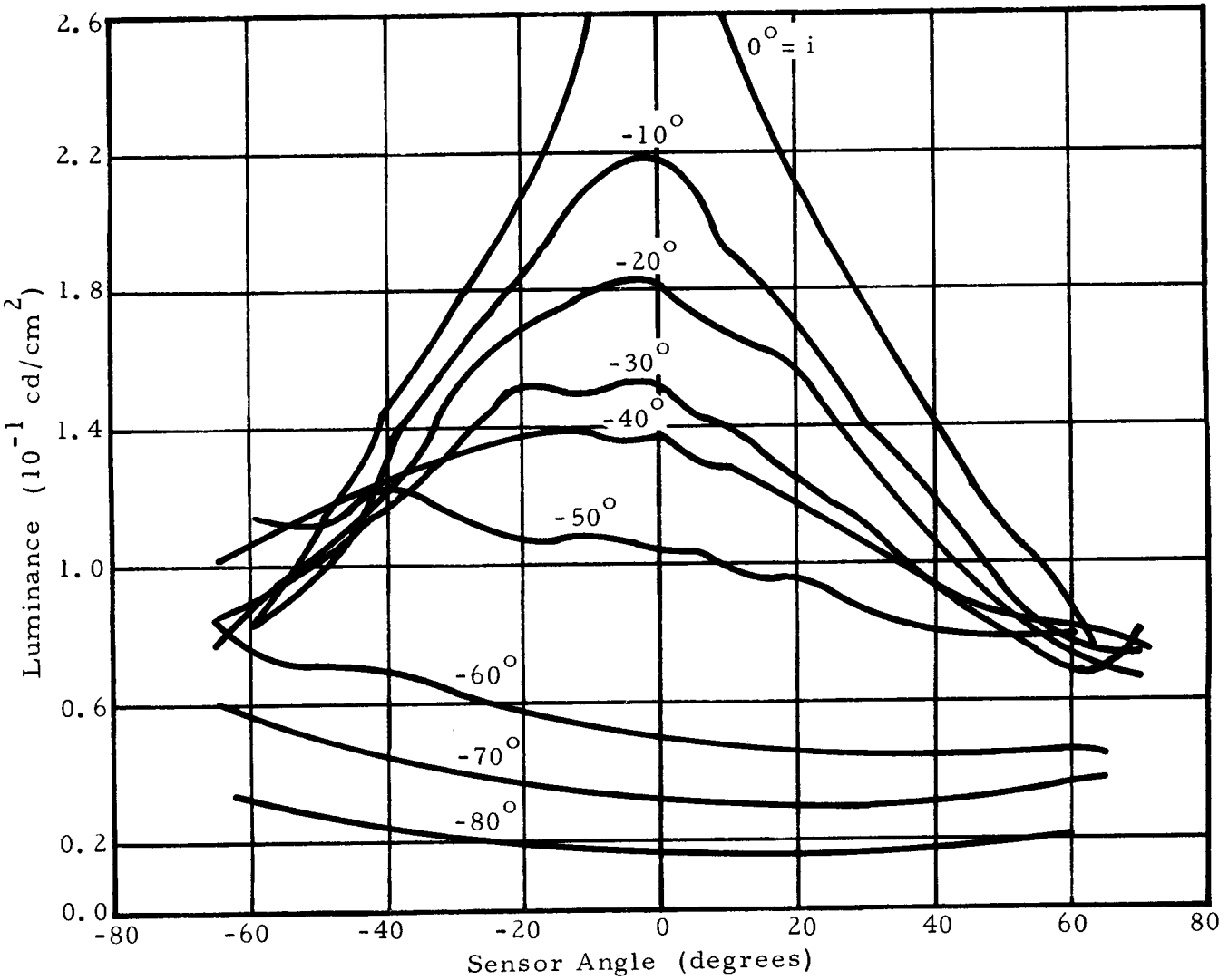

Figure 17 Empirical Noncoplanar (a = 70°) Photometric Curves Used in Slope Determination Experiment

angles taking on different values). In practice, the amount of error inherent in any remote photometric measurement makes it advisable to try to compute the two independently.

A series of photographic measurements was performed in order to evaluate the techniques, limitations, and accuracies of the photometric method. The lunar model was illuminated by sunlight with a clear sky and shielded as much as possible from scattered skylight. The sensor was a camera-film-target system with effective resolution approximating that of the high-resolution camera in the Lunar Orbiter. A number of photographs were taken for a range of source and sensor angles, but all were obtained for the noncoplanar geometry a = 70°. This was done because of time limitations and limitations of the facility, and it resulted in severe limitations in the accuracy of the final results. Three basic sun conditions were investigated: low sun angles with the sun near the model zenith (Figure 13); intermediate sun angle with the sun approximately 45° to the vertical (Figure 18); and low sun angles with the sun near the model horizon (Figure 19). A complete range of sensor angles was used for each source condition.

Source and sensor positions were measured with the Wild T3 theodolite, and accuracies of better than 0.02° were achieved. The true sensor angle for a given area was computed from the measured camera angle by standard trigonometric methods. The calibration procedure involved the use of a separate laboratory calibration after the photographs had been taken. A series of images of graduated intensity were placed along the edge of each film by The University of Michigan Observatory spot sensitometer. An independent calibration of the sensitometer was made, so that the actual illuminances at the film plane were known. Due to a mechanical defect in the timer, an uncertainty estimated to be as high as 25% was present in the calibration, which would be an extremely serious error. Apparently the actual error was considerably less than its maximum possible value, since reasonable results were obtained in the analysis.

From the calibrated spots, a set of D log E, or H and D, curves were generated for each film which allowed conversion of the image densities to equivalent film illuminances. The film densities were measured with a Jarrell-Ash scanning micro-densitometer with a viewing screen to allow accurate positioning of the image. The camera system was measured so that the lens transmission, exposure times, and f numbers were known, and with these parameters the film illuminances were directly converted to scene luminances.

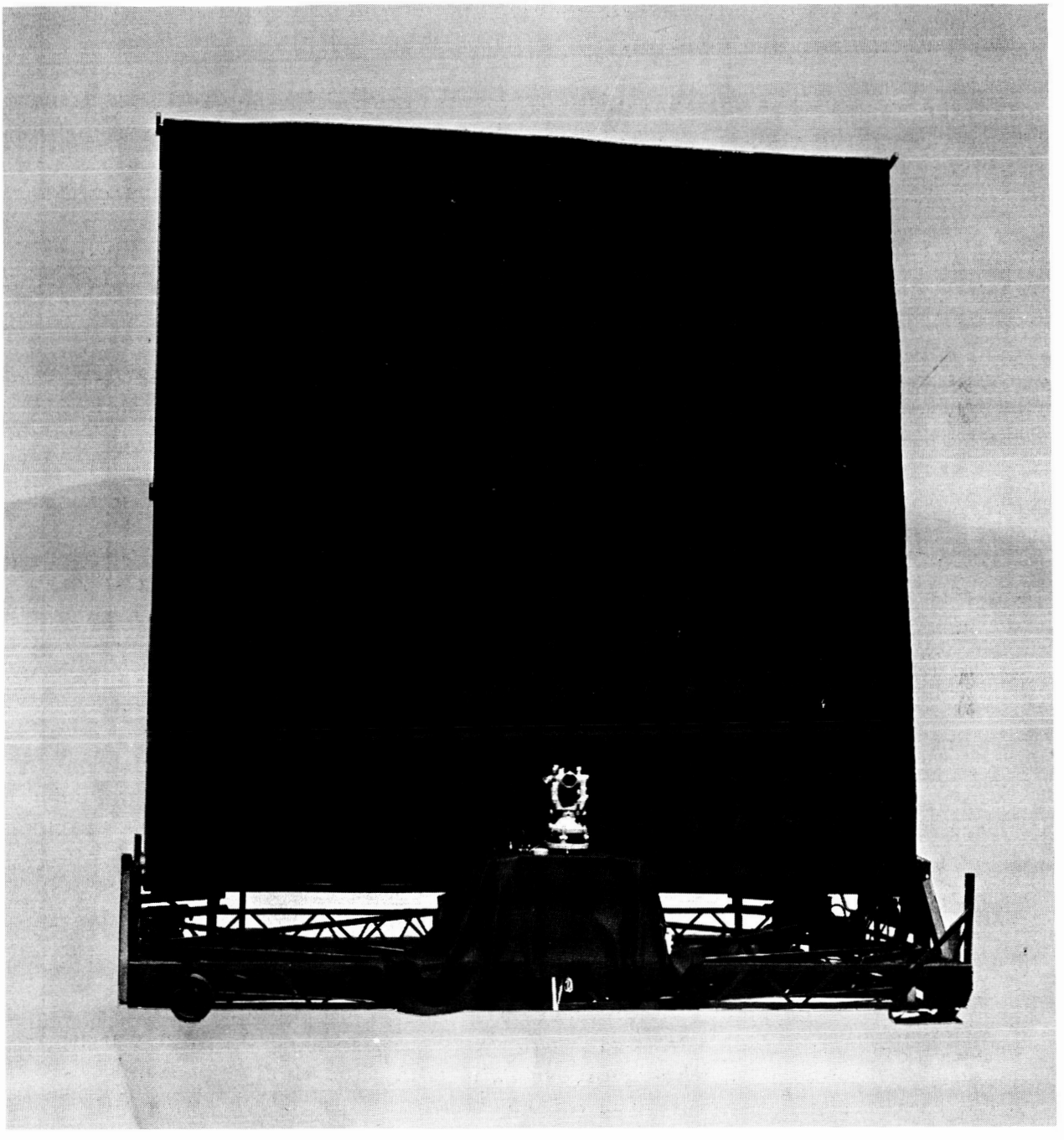

Figure 18 Appearance of Lunar Model for Intermediate Source Angle ($i = 43^{o}$) Photometric Experiment

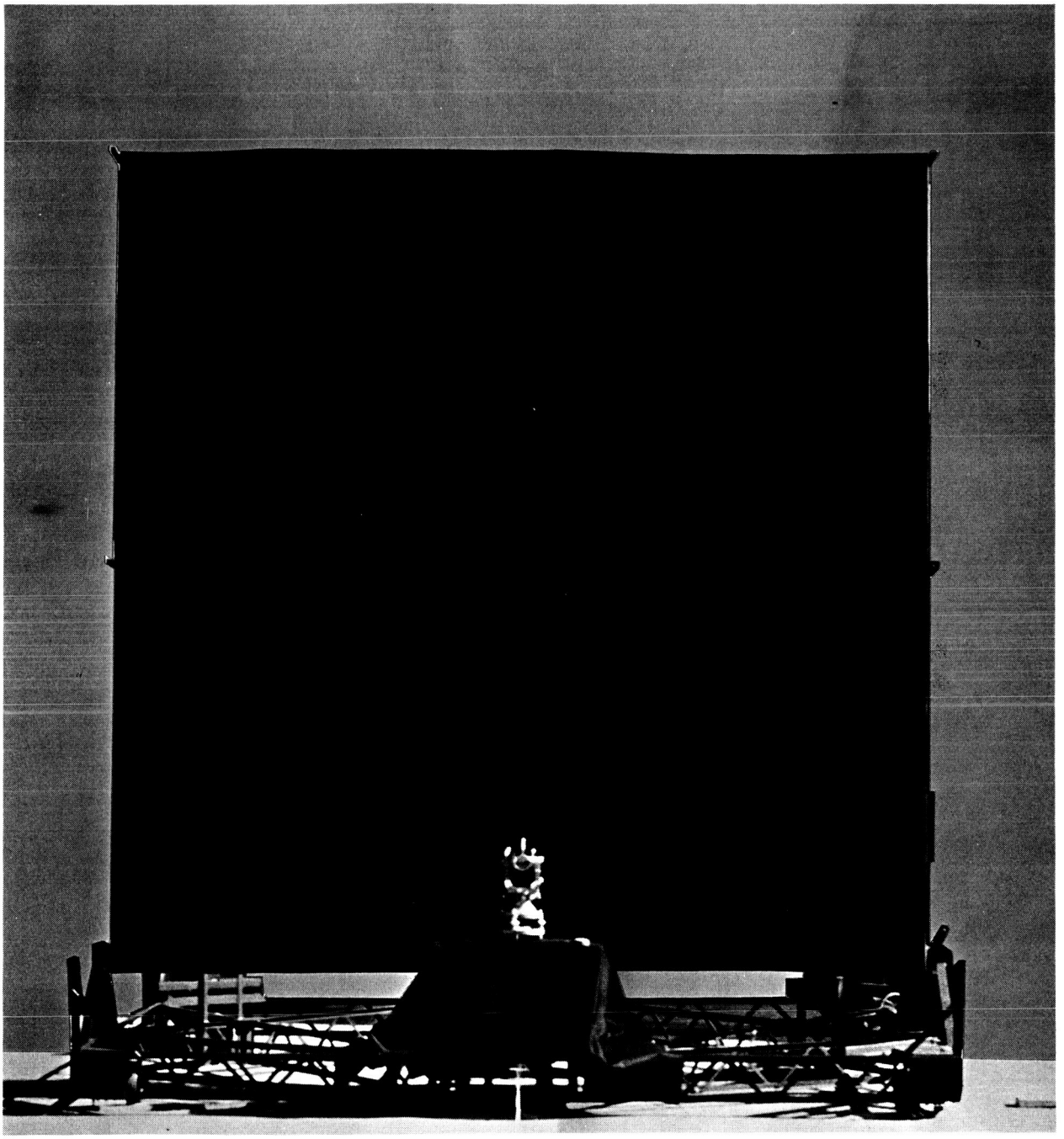

Figure 19 Appearance of Lunar Model for High Source Angle ($i = 88^{o}$) Photometric Experiment

The resulting photometric data consisted of plots of absolute luminance in candles/cm^2 as function of sensor angle. These plots contained at least two points representing the measured luminance at two sensor positions for a given sun angle. It is best, naturally, to have as large a range of sensor angles as possible in order to have a large luminance, curve but in the lunar situation, it is probable that at best two or three photographs of a given lunar feature will be obtained at a specified sun angle. For this reason, the luminance plots used to compute the slopes and albedos photometrically only contained three points corresponding to three closely spaced sensor positions.

By fitting the measured luminance curves to the a = 70° photometric curves for the lunar model (Figure 17) and obtaining the best match for for the data, both slopes and albedos were derived for eight areas on the model. The eight areas were chosen at well-spaced distances around the model, having slopes ranging from 0.78° up to 16.4° as determined from the contour map. All areas had albedos assumed to be equal to the mean normal albedo.

The results of the photometric experiment for a slope determination are tabulated in Table V with all slopes given in degrees. Because of the experimental problems, especially the interpolation to produce the a = 70° photometric function and the uncertainties in the calibration, the slope data are merely tabulated and no attempt is made to extract high precision results. The results indicate the following:

1. The photometric slopes are in most cases close to the true slope values.

2. The mean error is of the order of 3° for high source angles, with no serious errors, and the true slopes lying within the range of computed slopes.

3. The mean error for intermediate source angles is 5° or more, with no serious errors.

4. The errors for low source angles range from 1° to 50°, more values being close to true values than far away from it.

5. The range of error of computed slopes is small for low and intermediate source angles but large for small source angles.

TABLE V

SLOPE MEASUREMENTS BY THE PHOTOMETRIC METHOD

	Model Areas							
	1	2	3	4	5	6	7	8
True Slope (Degrees)	16.4	10.1	11.0	14.5	9.5 to 11.0	0.78	4.5	7.0
Photometric Slope Experiment 1 High Source Angles $i_{sun} = 88.5^{o}$	15.5±3	13.5±3	8.5±4	10.5^{+6}_{-4}	13.5±2	6.5^{+0}_{-2}	8.5^{+0}_{-2}	8.5^{+0}_{-4}
Photometric Slope - Experiment 2 Intermediate Source Angles, $i_{sun} = 43^{o}$	12.0±3	11.0±3	10.0±4	12.0±4	14±2 -4	15±2	13±3	13±3
Photometric Slope - Experiment 3 Low Source Angles $i_{sun} = 9^{o}$	29.0±10	9±10	69.±12	69.±5	9.9±10		9.0±0	19.0±10

These results should be considered as a demonstration of the capability of the lunar model and the photometric technique to provide a quantitative evaluation of procedures and accuracies. The actual results can not be relied upon as definitive due to the problems encountered in the experiment. However, they do indicate that the photometric technique is valid and that with careful control and good calibration data, accuracies at least of the order of 5^{o} can be achieved.

One problem that occurred for a specific geometry is that at low sun angles near the zenith, very small contrasts and luminance gradients are produced. This is a well-known characteristic of the lunar surface which is evident in telescopic views or photographs. It creates the problem of finding the same area in the various photographs in order to make the density measurement. Without an accurate control to measure the film coordinates exactly from some clearly recognizable feature, the interpreter has a very difficult job of locating the same exact position in each photograph. This factor probably was responsible for producing both the generally increased errors in slope for experiment 3 (low sun angles) and the few cases where huge errors occurred.

The same data are also used to compute the albedos of the same eight areas. These results are tabulated in Table VI and indicate errors of 10 to 40%. These values should be much more sensitive to errors in the film calibration then are the slope values, and they do seem to have been more seriously affected. The photometric technique is the only way of obtaining albedos, and its accuracy has been determined in other studies. Let it be merely concluded here that the results are approximately correct, but more careful calibration control is required to produce better accuracy.

From the results tabulated and from a direct examination of the photometric functions, the following conclusions can be drawn concerning the use of the photometric method:

1. With accurate calibration and photometric functions (3% or better), surface slopes should be photometrically measurable to 5^{o} for most source and sensor angles.

2. In this experiment, highest slope accuracies were obtained for high and intermediate source angles. Low source angles (near $i = 0^{o}$) produced generally increased slope errors and some very large errors.

TABLE VI

ALBEDO MEASUREMENTS USING THE PHOTOMETRIC METHOD

	Model Area							
	1	2	3	4	5	6	7	8
True Albedo	0.0515 ±0.0056	0.0515 ±0.0056	0.0515 ±0.0056	0.0515 ±0.0056	0.0515 ±0.0056	0.0515 ±0.0056	0.0515 ±0.0056	0.0515 ±0.0056
Photometric Albedo Experiment 1 - high source angles $i = 88.5^{o}$	0.055	0.063	0.045	0.055	0.042	0.016	0.062	0.069
Photometric Albedo Experiment 2 - Intermediate source angles $i = 43^{o}$	0.04	0.06	0.055	0.044	0.064	0.081	-	-

3. For the coplanar geometry ($a = 0^{\circ}$), all source and sensor positions should produce well-defined slope measurements. High source angles should be preferred because of the higher surface contrast. The best geometry for this case would be moderate-to-large source angles for small sensor angles, because in this region the photometric curves are well separated and their slopes are changing in a consistent manner. Also, the better contrasts will aid in evaluation.

4. For the noncoplanar geometry ($a = 90^{\circ}$), the source angle strongly influences the luminance, the sensor angle does so only slightly. The best procedure here would be to allow i to vary for a given value of ϵ. Also, a very bad geometry would be $0^{\circ} < |i| < 50^{\circ}$ for ϵ larger than $\pm 40^{\circ}$ as can be seen from Figure 11. The photometric curves overlap and intermingle here, and small photometric errors could produce relatively large slope errors. The best geometry for $a = 90^{\circ}$ would be $-30^{\circ} < \epsilon < +30^{\circ}$ for any source angle, i.e., camera near the zenith for any sun position.

5. For the intermediate noncoplanar geometry ($a = 70^{\circ}$), the results are similar to those for $a = 90^{\circ}$. In particular, from Figure 17 it can be seen that the region of $0^{\circ} < |i| < 50^{\circ}$ and ϵ larger than $\pm 40^{\circ}$ is a very confused region, with much crossover. This is an experimental illustration of the errors produced by an inaccurate photometric function. The best geometry for this case is also low sensor angle and arbitrary source angle.

5. The best lunar geometry for albedo measurement is a special case of the coplanar geometry which could be called "eclipse" geometry. Here the source and the sensor are directly aligned, and the reflectance is completely independent of surface slope, i and ϵ. For this special geometry, the normal albedo can be directly measured (since the photometric function equals 1.0) without any knowledge of the surface condition. For any other geometry than this, an estimate of the surface geometry must be made, because the photometric function enters the picture and must be calculated. In general, the best geometry for any value of a is to have ϵ as close to i as possible, i.e., to be as close to the reflectance peak as possible.

VI. CONCLUSIONS

The lunar model has a mean photometric function which exhibits all the qualitative characteristics of the lunar photometric function. The model provides an accurate tool which can be used to make quantitative experimental evaluations of techniques and procedures which may be used for remote analysis of the lunar surface. There are significant quantitative differences in the photometric response of the model from the lunar surface, the most significant being a large decrease in the back-scattering peak with increasing source angles.

The calibration accuracies for the model are ±10% for the mean normal albedos, ±3% for the photometric functions, and ±1/4° for the slope variance areas. For small source angles, the mean error in the photometric function may be as high as ±5%, due to experimental factors. An accurate contour map of the model is presented, and tables of slopes, normal albedos, and photometric functions for two geometries are included.

The optical studies of the lunar model demonstrate that it is capable of producing quantitative experimental data which can be used to compare various techniques and procedures. Because of experimental deficiencies, the photogrammetric results indicated a mean error of 5 to 10%, but this is an upper limit. Low sun angles (sun close to the zenith) were found to create maxim difficulty and resultant error in photogrammetric measurements. The photometric experiments demonstrated that high and intermediate sun angles produced reasonably accurate, consistent measurements of surface slope by the photometric method. Larger mean errors and some serious errors resulted from low sun angle geometry. Within the severe limitations of this experiment, slope accuracies of 5° were attained, and this is a strong indication that a carefully controlled experiment could produce better slope accuracies. An evaluation of various source sensor geometries was carried out; while no major effects are present for coplanar geometry, the noncoplanar geometry has very definite optimum conditions.

VII. BIBLIOGRAPHY

A. Hapke, B., 1963, J. Geophys. Res., 68, 4571.

B. Hapke, B., 1966, Astron. J., 71, 333.

C. Parker, H. M., Mayo, T. T., Birney, D. S. and McCloskey, G., 1964, NASA Report No. N64-18439.

D. Herriman, A. G., Washburn, H. W. and Willingham, D. E., 1963, JPL Tech. Report No. TR 32-384.

E. Willingham, D., JPL Tech. Report No. 32-664.